Acta Geophysica (2024) 72:1819–1845
https://doi.org/10.1007/s11600-023-01184-4

RESEARCH ARTICLE - APPLIED GEOPHYSICS

Magnetic inversion approach for modeling data acquired across faults: various environmental cases studies

Khalid S. Essa[1] · Eid R. Abo-Ezz[2] · N. L. Anderson[3] · Omar A. Gomaa[1] · Mahmoud Elhussein[1]

Received: 23 January 2023 / Accepted: 29 August 2023 / Published online: 27 October 2023

Abstract
An effective extension to the particle swarm optimizer scheme has been developed to visualize and modelize robustly magnetic data acquired across vertical or dipping faults. This method can be applied to magnetic data sets that support various investigations, including mining, fault hazards assessment, and hydrocarbon exploration. The inversion algorithm is established depending on the second horizontal derivative technique and the particle swarm optimizer algorithm and was utilized for multi-source models. Herein, the inversion method is applied to three synthetic models (a dipping fault model contaminated without and with different Gaussian noises levels, a dipping fault model affected by regional anomaly, and a multi-source model) and three real datasets from India, Australia, and Egypt, respectively. The output models confirm the inversion approach's accuracy, applicability, and efficacy. Also, the results obtained from the suggested approach have been correlated with those from other methods published in the literature.

Keywords Faults · Modeling · Magnetic anomalies · Interpretation

Introduction

Magnetic surveying is a crucial subsurface imaging tool. The tool is routinely used to image subsurface geological structures (An and Di 2016; Araffa and Bedair 2021; Ugbor et al. 2021; Essa et al. 2022), and in support of hydrocarbon exploration (Saunders et al. 1991; Abubakar et al. 2015; Ivakhnenkoa et al. 2015; Innocent et al. 2019; Abdullahi and Kumar 2020), mineral exploration and mining (Mandal et al. 2015; Ghanati el al. 2017; Akinlalu et al. 2018; Biswas 2018; Essa and Elhussein 2019; Melo et al. 2020; Mehanee et al. 2021; Essa and Diab 2022a), geothermal energy (Abraham et al. 2014; Shirani et al. 2020; Hosseini et al. 2021), archeological studies (Scollar et al. 1986; Tsokas and Papazachos 1992; Gerard-Little et al. 2012; Linford et al. 2019), the detection of sinkholes (Balkaya et al. 2012), and other environmental and engineering investigations (Reynolds 2011; Niederleithinger et al. 2012; Liu et al. 2021).

Magnetic inversion is a significant geophysical approach that provides beneficial insights into the subsurface in many kinds of fields. It entails analyzing magnetic field data for the purpose of figuring out fault parameters, identifying geological structures, and outlining subsurface features. Magnetic inversion improves in gaining an understanding of fault systems, their geometries, and orientations in geology and tectonics. Researchers can acquire insights into the behavior and potential seismic risks connected with faults by precisely predicting fault characteristics such as dip angles, depths, and slip rates. This data is critical for determining the stability of geological formations, forecasting earthquakes, and planning infrastructure development in seismically active areas.

Multiple inversion methods were developed to model magnetic data. Each method employs a slightly different approach. The methods include the graphical technique, which is based upon a few distinct locations on the magnetic anomaly profile (Gay 1963; Subrahmanyam and Prakasa Rao 2009), the characteristic curve technique (Hutchison 1958;

Edited by Prof. Ivana Vasiljevic (ASSOCIATE EDITOR) / Prof. Gabriela Fernández Viejo (CO-EDITOR-IN-CHIEF).

✉ Khalid S. Essa
khalid_sa_essa@cu.edu.eg; essa@sci.cu.edu.eg

1 Geophysics Department, Faculty of Science, Cairo University, P.O. 12613, Giza, Egypt

2 Department of Physics, College of Science and Humanities, Prince Sattam Bin Abdulaziz University, 11942 Al-Kharj, Saudi Arabia

3 Geosciences and Geological and Petroleum Engineering Department, Missouri University of Science and Technology, P.O. 65409, Rolla, USA

Grant and Martin 1966; Abdelrahman and Essa 2005), the least-square approach (Abdelrahman et al. 2007; Tlas and Asfahani 2011), the Euler deconvolution technique (Li 2003; Dewangan et al. 2007), the Werner deconvolution approach (Stagg et al. 1989; Hansen 2005; Usman et al. 2014), the gradient technique (Abdelrahman et al. 2003; Essa and Elhussein 2017), the analytical-signal technique (Nabighian 1972; Salem 2005; Aydin 2008), the tilt angle approach (Miller and Singh 1994; Essa et al. 2018; Pham et al. 2019; Elhussein and Shokry 2020), and the Fourier-transform technique (Gudmundsson 1966; Gupta 1988; Olurin et al. 2017). The disadvantages of these listed approaches are that they are sensitive to noise and dependent on prior information.

More recently, new artificial intelligence-based methods have been developed to model magnetic data. These methods are based on approaches including particle swarm optimizer (Liu et al. 2017; Essa and Elhussein 2020; Pace et al. 2021; Essa et al. 2023), the genetic algorithm technique (Currenti et al. 2007; Montesinos et al. 2016; Kaftan 2017), the simulated annealing approach (Biswas 2016, 2018; Biswas and Acharya 2016), the neural network approach (Hajian et al. 2012; Deng et al. 2022), Bat algorithm (Essa and Diab 2022b), the ant colony technique (Kushwaha et al. 2018), and the barnacle mating (Ai et al. 2022).

This work develops a method for modeling magnetic data acquired across faults. The approach employed is as follows. Initially, the second horizontal derivative helps confiscate the influence of regional background. The particle swarm optimizer scheme is then exploited to derivative anomalies to gauge the different fault structure parameters (amplitude coefficient (A_c), fault angle (θ), effective magnetization vector dip angle (α), depths to the upper side of the fault (h_1) and the lower side of the fault (h_2), and the fault origin (w)). Three synthetic models and three real field cases were examined from India, Australia, and Egypt to verify this method's efficacy.

There are numerous merits when utilizing PSO for determining fault parameters. For starters, PSO is a global search algorithm, which implies it can identify the objective function's global minimum regardless of whether the objective function contains several local minima. Second, PSO is simple to establish and requires few parameters. Third, PSO is being noticed to be useful in a range of applications, including the estimation of fault parameters. PSO can be sluggish to converge, especially when dealing with complex issues. Using horizontal derivatives of magnetic data to boost PSO convergence is one method. Horizontal derivatives can be utilized to lessen the effect of the regional magnetic field, allowing PSO to identify the global minimum more easily.

The paper is divided into four sections. The methodology and the corresponding algorithm are first detailed. The second section illustrates the utilization of three synthetic models. The third section illustrates the use of three real data. Finally, the paper ends with conclusions.

The methodology

Ideally, magnetic field data acquired across a feature of interest is comprised of the regional magnetic field (background) and the superposed residual anomaly (target anomaly) (Pawlowski 1994; Essa 2021). The following formula can give this magnetic field:

$$M(x_i) = M_{res}(x_i) + Z(x_i). \tag{1}$$

Equation (1) shows the total measured magnetic field represented by $M(x_i)$, $M_{\text{res}}(x_i)$ is a residual anomaly, $Z(x_i)$ is a regional magnetic field (background), and x_i is the observation data point.

In this study, the residual anomalies are generated by a vertical or dipping fault. The particle swarm optimizer technique examined residual anomalies, detached from the total magnetic anomaly utilizing the second horizontal derivative approach.

Forward modeling of fault structure and a second horizontal derivative scheme

The magnetic anomaly measured across arbitrarily dipping magnetized fault at any point (x_i) is given by (Murthy et al. 2001; Ekinci et al. 2019). (Fig. 1):

$$M_{\text{res}}(x_i) = 2A_c \sin\theta \left\{ \cos(\theta+\alpha')(\theta_2-\theta_1) + \sin(\theta+\alpha') \ln\left(\sqrt{\frac{\left((x_i-w)+(h_2-h_1)\cot(\theta)\right)^2+h_2^2}{(x_i-w)^2+h_1^2}} \right) \right\}, \quad i = 0,1,2,3,\ldots,P, \tag{2}$$

where P is the data numbers; A_c is the amplitude coefficient (nT) and is given by:

Fig. 1 A sketch diagram displays the dipping fault's geometric structure and parameters

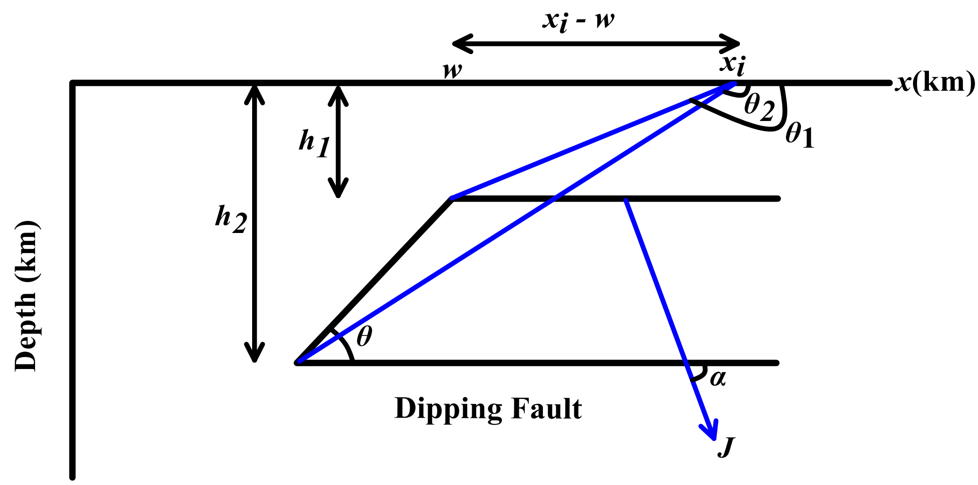

$$A_c = J \cdot \sqrt{1 - \left((\cos(\beta))^2 \cdot (\cos(\gamma))^2\right)},$$

J signifies the effective magnetization intensity (nT); and β is the strike of the 2-D fault structure measured east or west from the magnetic north ($0° \leq \beta \leq 90°$). γ is the direction of measurements (which equals zero in the case of the horizontal component, $\pi/2$ in the vertical component, and I (inclination angle) in the case of the total field). θ is the fault angle (degree). α' is given by: $\alpha' = \alpha - \tan^{-1}(\sin(\beta) \cdot \cot(\gamma))$. α is the effective magnetization vector dip angle (degree). w is the fault origin (km). h_2 denotes the depth to the lower side of the fault (km). h_1 represents the depth to the upper side of the fault (km); θ_2 is given by: $\theta_2 = \frac{\pi}{2} + \tan^{-1}\left(\frac{(x_i-w)+(h_2-h_1)cot\theta}{h_2}\right)$, and θ_1 is given by:

$$\theta_1 = \begin{cases} \frac{\pi}{2} + \tan^{-1}\left(\frac{x_i-w}{h_1}\right), & \text{in case } h_1 \neq 0 \\ \frac{\pi}{2}\left(1 + \frac{x_i-w}{|x_i-w|}\right), & \text{in case } h_1 = 0, x_i \neq 0 \cdot \\ \frac{\pi}{2}, & \text{in case } h_1 = 0, x_i = 0. \end{cases}$$

For vertical faults ($\theta = 90^o$), the magnetic anomaly (Eq. 2) can be given by the following formula:

$$M_{\text{res}}(x_i) = 2A_c\left\{-\sin(\alpha')(\theta_2 - \theta_1) + \cos(\alpha')\ln\left(\sqrt{\frac{(x_i - w)^2 + h_2^2}{(x_i - w)^2 + h_1^2}}\right)\right\}, \quad i = 0, 1, 2, 3, ..., P. \tag{3}$$

To remove the regional background $Z(x_i)$, the second horizontal derivative operator was applied to Eq. 1; for three observation points along the magnetic profile ($x_i - 2s$, x_i, $x_i + 2s$), the second horizontal derivative ($M_{xx}(x_i, s)$) can be given by (Essa and Elhussein 2017):

$$M_{xx}(x_i, s) = \frac{M(x_i + 2s) - 2M(x_i) + M(x_i - 2s)}{4s^2}, \tag{4}$$

where $s = 1, 2, 3, \ldots, N$ separation units are graticule spacings, and x_i is the observation data point.

Inversion approach

The proposed method is based on the particle swarm optimizer scheme. This algorithm was recognized primarily by Eberhart and Kennedy (1995). The particle swarm optimizer scheme is applied nowadays to different geophysical applications (Srivastava and Agarwal 2010; Xiong and Zhang 2015; Ekinci et al. 2019; Essa and Géraud 2020; Essa et al. 2021; Elhussein 2021). The particle swarm optimizer approach is stochastic. In this application, the approach can be explained metaphorically by considering a group of birds searching for food. Models can represent the birds; for each model, there is a velocity vector and a location vector collectively representing the parameter's value. The inversion is initiated by giving random models for the swarm utilizing the possible ranges of the different variables. The velocity and position of the different models are iteratively updated using the following formulas:

$$V_i^{k+1} = c_3 V_i^k + c_1 \text{rand1}\left(K_{\text{best}} - X_i^{k+1}\right) + c_2 \text{rand2}\left(L_{\text{best}} - X_i^{k+1}\right), \tag{5}$$

$$X_i^{k+1} = X_i^k + V_i^{k+1}. \tag{6}$$

Equation (6) shows X_i^k and V_i^k that represent the place and velocity of the particle i, respectively, at iteration k; rand1 and rand2 represent two randomized numbers in the range [0,1]; c_1 and c_2 are cognitive and social coefficients that are usually equal to 2 represented by Eq. (5) (Singh and Biswas 2016; Essa and Elhussein 2018; Pace et al. 2021); c_3 is the inertial coefficient that controls the model's velocity and takes on a value of less than one; and K_{best} is the best location which got by an individual model, while L_{best} is the best global location reached by any model in the swarm. Afterward, the best solution (K_{best}) and the global best solution (L_{best}) are stored in memory. The model's velocity and position are updated during an iterative process that ends when the convergence occurs (Venter and Sobieski 2002). The convergence is reached by optimizing the following objective function (Ψ_{obj}):

$$\Psi_{\text{obj}} = \frac{1}{P}\sum_{i=1}^{P}\left[M^{\text{O}}_{\text{res }i}(x_i) - M^{\text{c}}_{\text{res }i}(x_i)\right]^2, \tag{7}$$

P are the data points numbers, $M^{\text{O}}_{\text{res}i}$ are the observed magnetic anomaly, and $M^{\text{c}}_{\text{res}i}$ are the calculated magnetic anomaly at the different data points x_i.

The fault structure parameters (A_c, θ, α, h_1, h_2, and w) are inverted by minimizing (Eq. 7) for the several graticule spacings (s values) applied in the separation of residual anomaly through applying the second horizontal derivative (Eq. 4); the solution of the different parameters is reached by taking the average value ($\mathcal{G}$) of the inverted parameters for numerous s values. The RMS error (root mean square) is deliberated by using the following equation:

$$\text{RMS} = \sqrt{\frac{1}{P}\sum_{i=1}^{P}\left[M^{\text{O}}_{\text{res}\,i}(x_i) - M^{\text{c}}_{\text{res}\,i}(x_i)\right]^2}. \tag{8}$$

Figure 2 shows the flowchart, which explains the estimation of the different parameters using the employed approach.

Synthetic models

Three theoretical models were generated to assess and verify the method's applicability, accuracy, and efficacy.

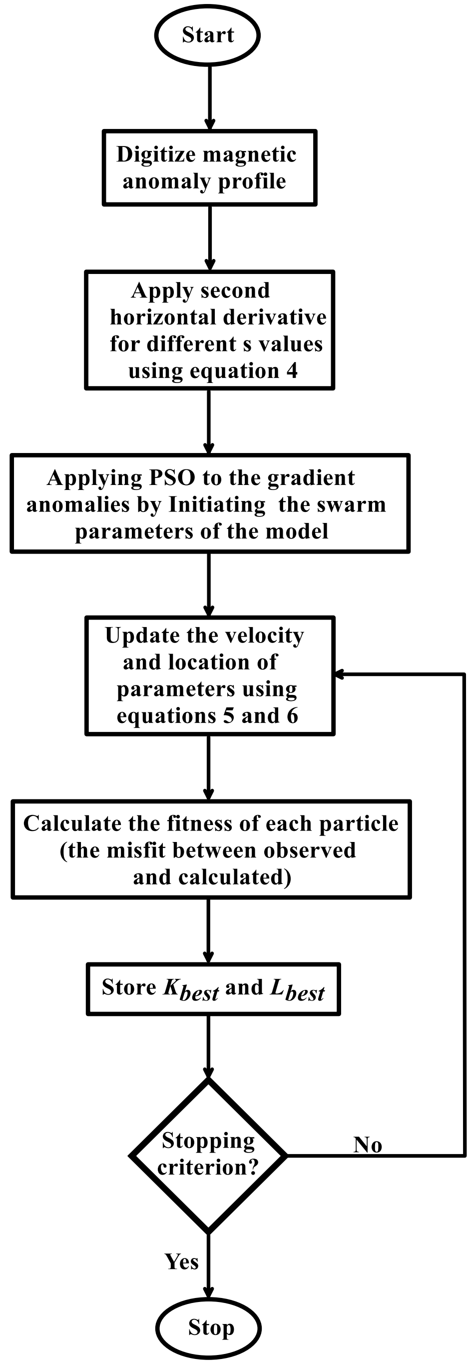

Fig. 2 Flowchart showing the complete steps for predicting the fault's parameters using the proposed approach

Model I: Simple dipping fault magnetic anomaly without and with noise

A 120 km magnetic anomaly profile was generated without noise by dipping fault using $A_c = 300$ nT, $\theta = 70°$, $\alpha = 40°$, $h_1 = 4$ km, $h_2 = 10$ km, and $w = 60$ km (Fig. 3a). The profile was filtered by applying the second horizontal derivative

Fig. 3 **a** A synthetic noise-free magnetic anomaly produced by dipping fault model with $A_c = 300$ nT, $\theta = 70°$, $\alpha = 40°$, $h_1 = 4$ km, $h_2 = 10$ km, $w = 60$ km, and profile length = 120 km. The model structure and the predicted anomaly are also displayed. **b** Second horizontal derivative anomalies are calculated from the anomaly in Fig. 3a

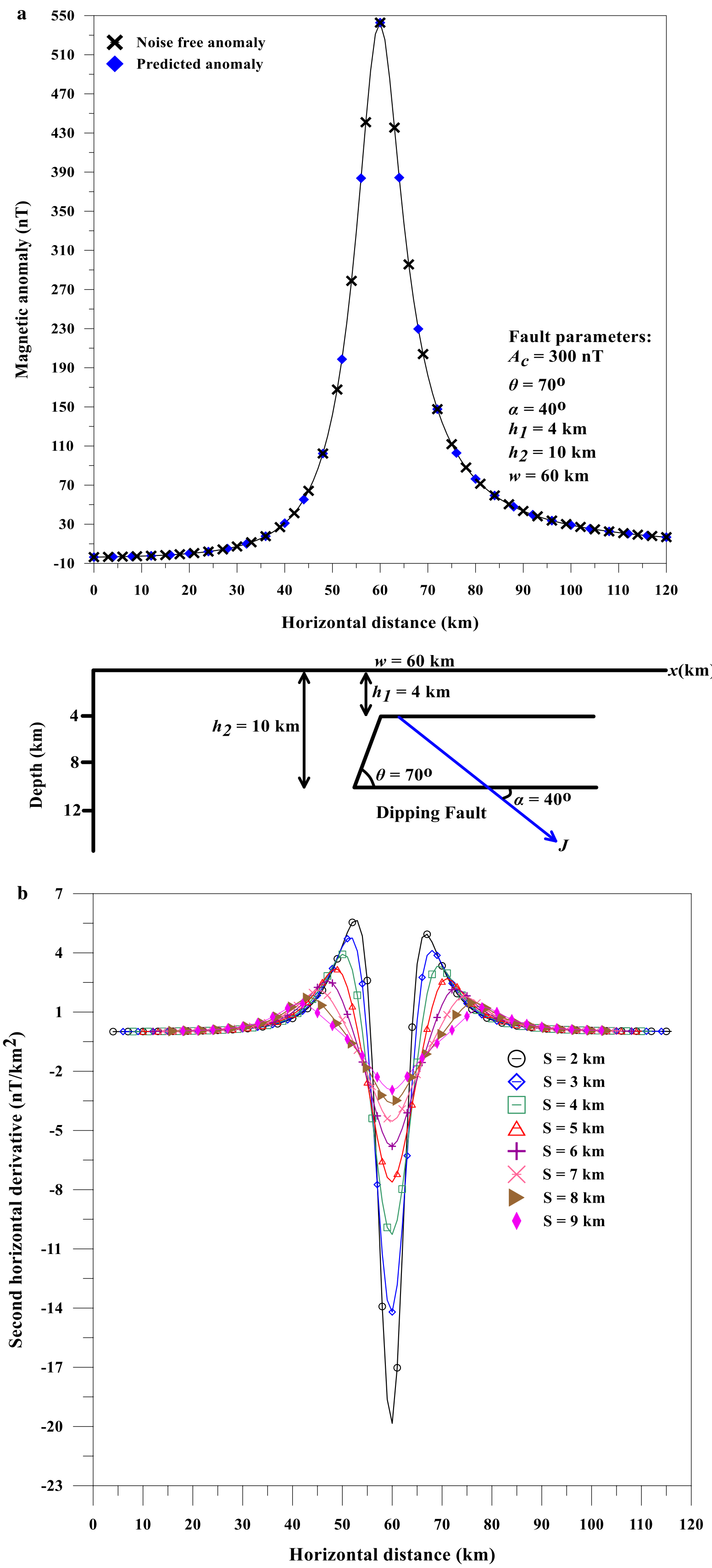

Table 1 Results of the global particle swarm optimization approach applied to second horizontal derivative anomalies for the magnetic anomaly profile (120 km) due to the dipping fault model (A_c = 300 nT, θ = 70°, α = 40°, h_1 = 4 km, h_2 = 10 km, and w = 60 km), without and with 15% and 20% noise

Parameters	Used ranges	Using global particle swarm inversion for the magnetic derivative data										
		s = 2 km	s = 3 km	s = 4 km	s = 5 km	s = 6 km	s = 7 km	s = 8 km	s = 9 km	Average value (GƆ)	Error (%)	RMS error (nT)
Results (noise free)												
A_c(nT)	50–700	300	300	300	300	300	300	300	300	300 ± 0	0	0
θ(degree)	30–100	70	70	70	70	70	70	70	70	70 ± 0	0	
α(degree)	20–70	40	40	40	40	40	40	40	40	40 ± 0	0	
h_1(km)	1–9	4	4	4	4	4	4	4	4	4 ± 0	0	
h_2(km)	7–15	10	10	10	10	10	10	10	10	10 ± 0	0	
w (km)	50–70	60	60	60	60	60	60	60	60	60 ± 0	0	
Results (using 15% noise)												
A_c(nT)	50–700	325.34	310.70	292.69	295.98	304.21	297.13	305	302.00	303.88 ± 10.40	1.29	8.91
θ(degree)	30–100	67.33	68.39	66.10	71.62	72.59	68.58	69.46	70.80	69.36 ± 2.20	0.91	
α(degree)	20–70	43.7	37.6	42.10	41.15	40.9	39.5	39.2	38.6	40.34 ± 2.00	0.85	
h_1(km)	1–9	3.7	4.3	4	3.8	3.6	3.9	4.1	4.1	3.94 ± 0.23	1.5	
h_2(km)	7–15	10.5	9.5	9.6	10.2	10.3	10.4	9.8	10.2	10.06 ± 0.38	0.6	
w (km)	50–70	60.26	60.33	60.90	59.98	60.04	60.19	60.14	59.70	60.19 ± 0.35	0.32	
Results (using 20% noise)												
A_c(nT)	50–700	295.16	297	307	311.18	328.42	324.60	320.39	294.84	309.82 ± 13.57	3.27	21.71
θ(degree)	30–100	64.17	75	72.51	67.81	66.99	73.70	71.90	74.14	70.78 ± 3.94	1.11	
α(degree)	20–70	45.2	41.4	43.05	44	41.2	38.9	39.5	39.8	41.6 ± 2.3	4	
h_1(km)	1–9	3.7	3.6	3.9	3.5	3.6	3.8	4.1	3.7	3.74 ± 0.19	6.5	
h_2(km)	7–15	10.4	10.5	10.3	10.4	10.5	10.2	10.1	10.2	10.33 ± 0.15	3.3	
w (km)	50–70	60.06	59.16	60.11	61.14	60.38	59.35	59.30	59.45	59.87 ± 0.68	0.22	

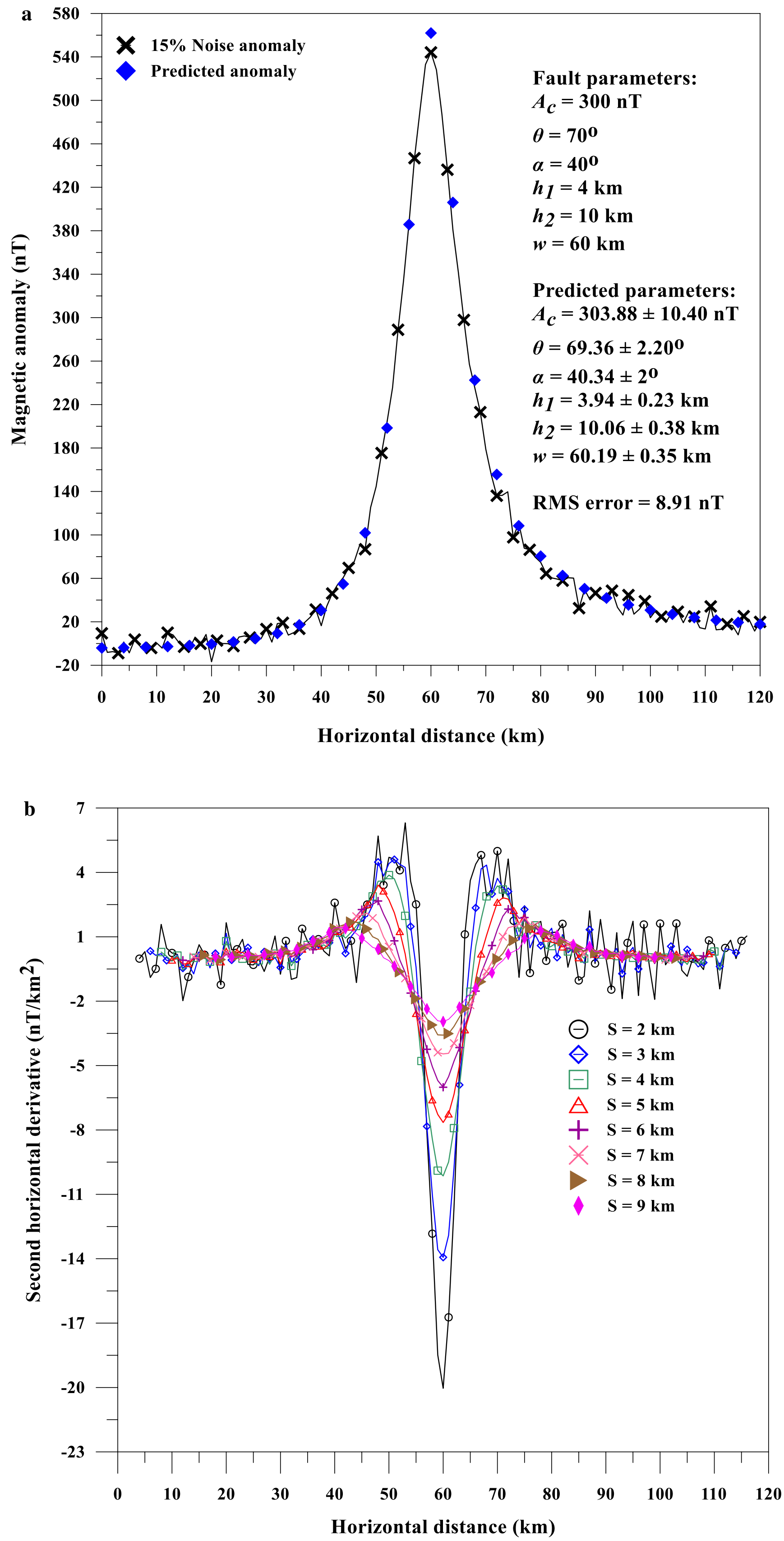

Fig. 4 **a** The magnetic anomaly mentioned in Fig. 3a is tainted with a 15% Gaussian noise and the predicted anomaly. **b** Second horizontal derivative anomalies are calculated from the noisy magnetic anomaly in Fig. 4a

Fig. 5 **a** The magnetic anomaly in Fig. 3a is contaminated with a 20% Gaussian noise and the predicted anomaly. **b** Second horizontal derivative anomalies are calculated from the noisy magnetic anomaly in Fig. 5a

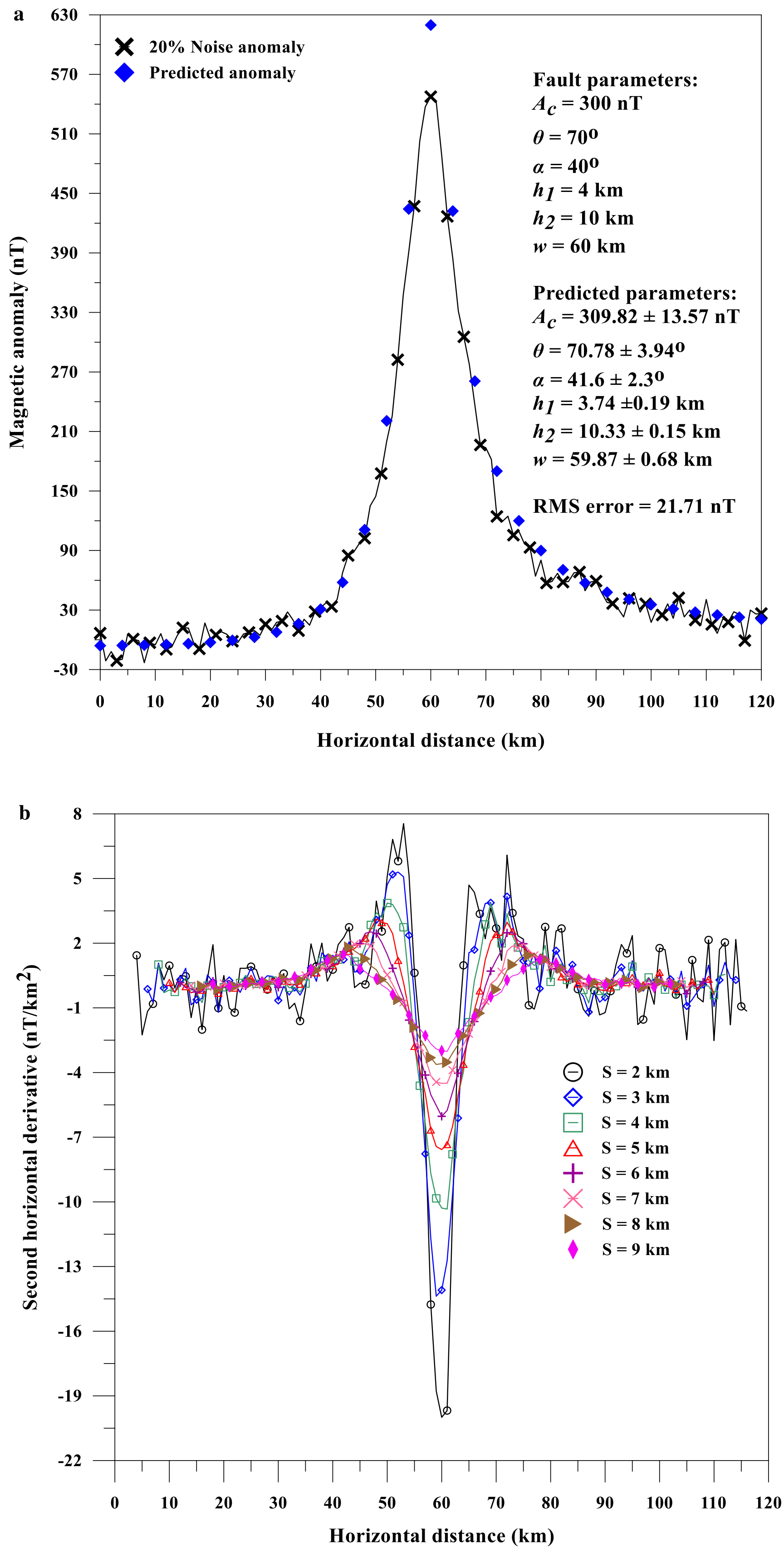

Fig. 6 **a** A composite magnetic anomaly of dipping fault (A_c = 450 nT, θ = 100°, α = 50°, h_1 = 5 km, h_2 = 16 km, w = 75 km, and profile length 120 km) and first-order regional anomaly ($2x_i$ – 15). The model structure and the predicted anomaly are also displayed. **b** Second horizontal derivative anomalies are calculated from the anomaly in Fig. 6a

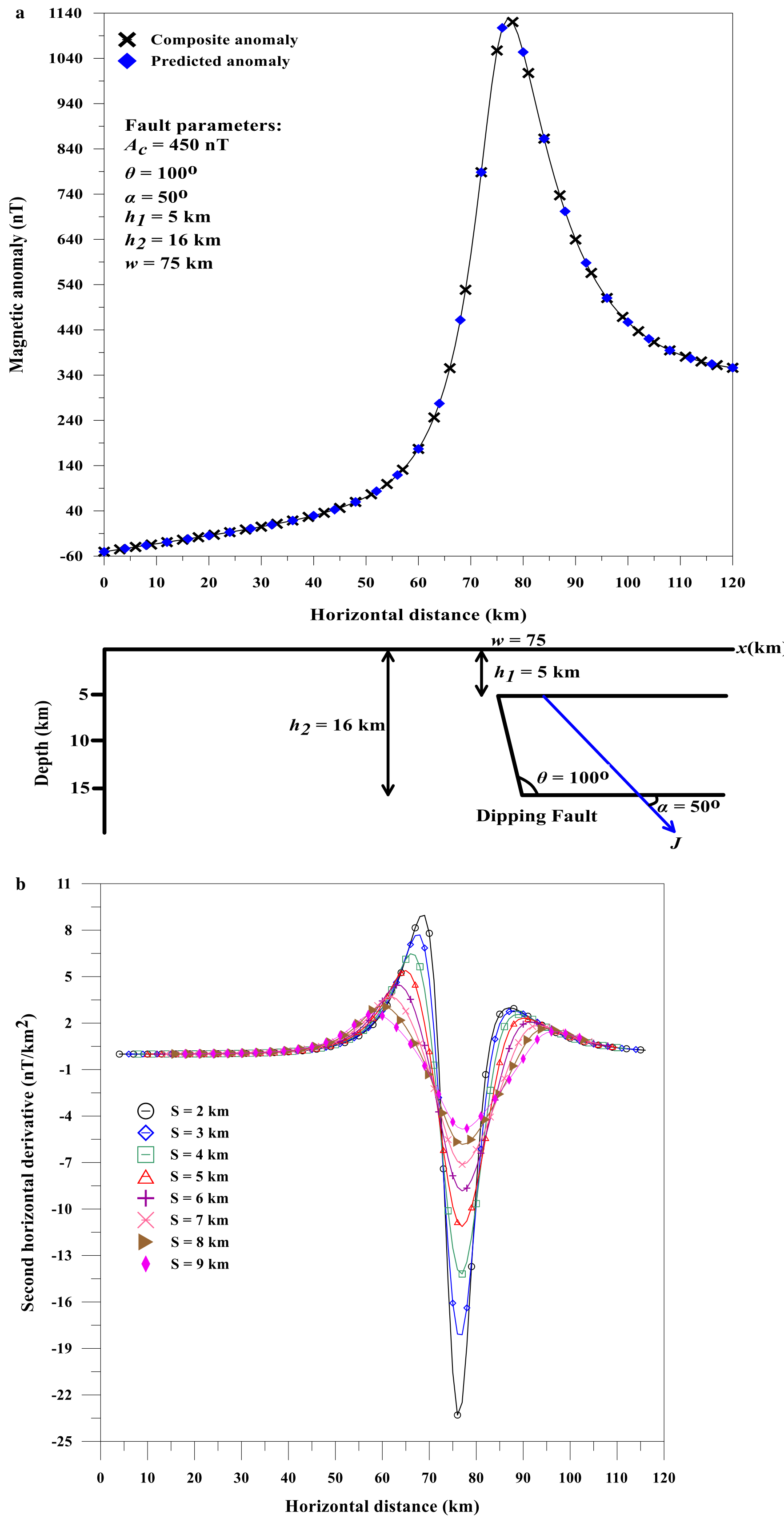

Table 2 Results of the global particle swarm optimization approach applied to second horizontal derivative anomalies for the magnetic anomaly profile (120 km) due to the composite anomaly of the dipping fault model ($A_c = 450$ nT, $\theta = 100°$, $\alpha = 50°$, $h_1 = 5$ km, $h_2 = 16$ km, and $w = 75$ km) and first-order regional anomaly ($2x_i - 15$), without and with 20% noise

Parameters	Used ranges	Using global particle swarm inversion for the magnetic derivative data										
		s = 2 km	s = 3 km	s = 4 km	s = 5 km	s = 6 km	s = 7 km	s = 8 km	s = 9 km	Average value (GƆ)	Error (%)	RMS error (nT)
Results (Noise free)												
A_c(nT)	100–800	450	450	450	450	450	450	450	450	450 ± 0	0	0
θ(degree)	50–170	100	100	100	100	100	100	100	100	100 ± 0	0	
α(degree)	20–85	50	50	50	50	50	50	50	50	50 ± 0	0	
h_1(km)	1–9	5	5	5	5	5	5	5	5	5 ± 0	0	
h_2(km)	8–22	16	16	16	16	16	16	16	16	16 ± 0	0	
w (km)	65–85	75	75	75	75	75	75	75	75	75 ± 0	0	
Results (using 20% noise)												
A_c(nT)	100–800	446.97	467	459.89	463.22	465	457.41	460.68	464	460.52 ± 6.27	2.34	21.04
θ(degree)	50–170	104.67	103.64	98.86	104.77	103.09	102.05	98.69	103.93	102.46 ± 2.44	2.46	
α(degree)	20–85	54.1	49.2	49.9	47.2	48.4	48.1	52.6	49.3	49.85 ± 2.35	0.3	
h_1(km)	1–9	5.3	4.6	4.7	4.6	4.5	4.6	5	5.3	4.83 ± 0.33	3.4	
h_2(km)	8–22	15.7	16.3	16.4	16.5	16.1	16.5	15.9	15.5	16.11 ± 0.38	0.69	
w (km)	65–85	74.29	74.79	75.07	74.50	74.16	74.75	75.54	74.82	74.74 ± 0.44	0.35	

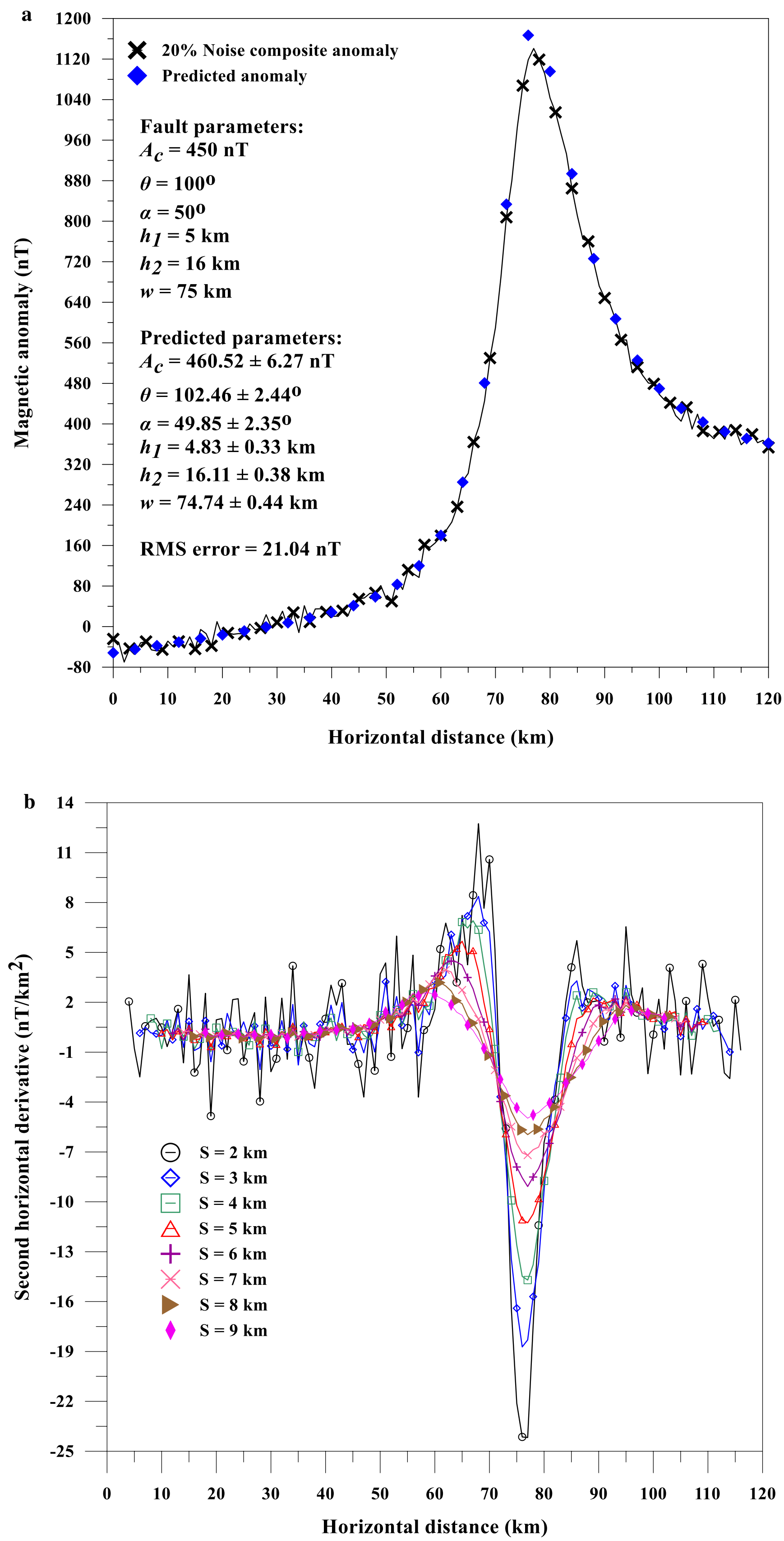

Fig. 7 **a** The magnetic anomaly mentioned in Fig. 6a is contaminated with a 20% Gaussian noise and the predicted anomaly. **b** Second horizontal derivative anomalies are calculated from the noisy magnetic anomaly in Fig. 7a

Fig. 8 **a** A composite magnetic anomaly of dipping fault (A_c = 350 nT, θ = 50°, α = 70°, h_1 = 7 km, h_2 = 17 km, w = 50 km, and profile length 140 km) and another dipping fault model (A_c = 250 nT, θ = 75°, α = 70°, h_1 = 2 km, h_2 = 7 km, w = 100 km, and profile length 140 km). The model structure and the predicted anomaly are also displayed. **b** Second horizontal derivative anomalies are calculated from the anomaly in Fig. 8a

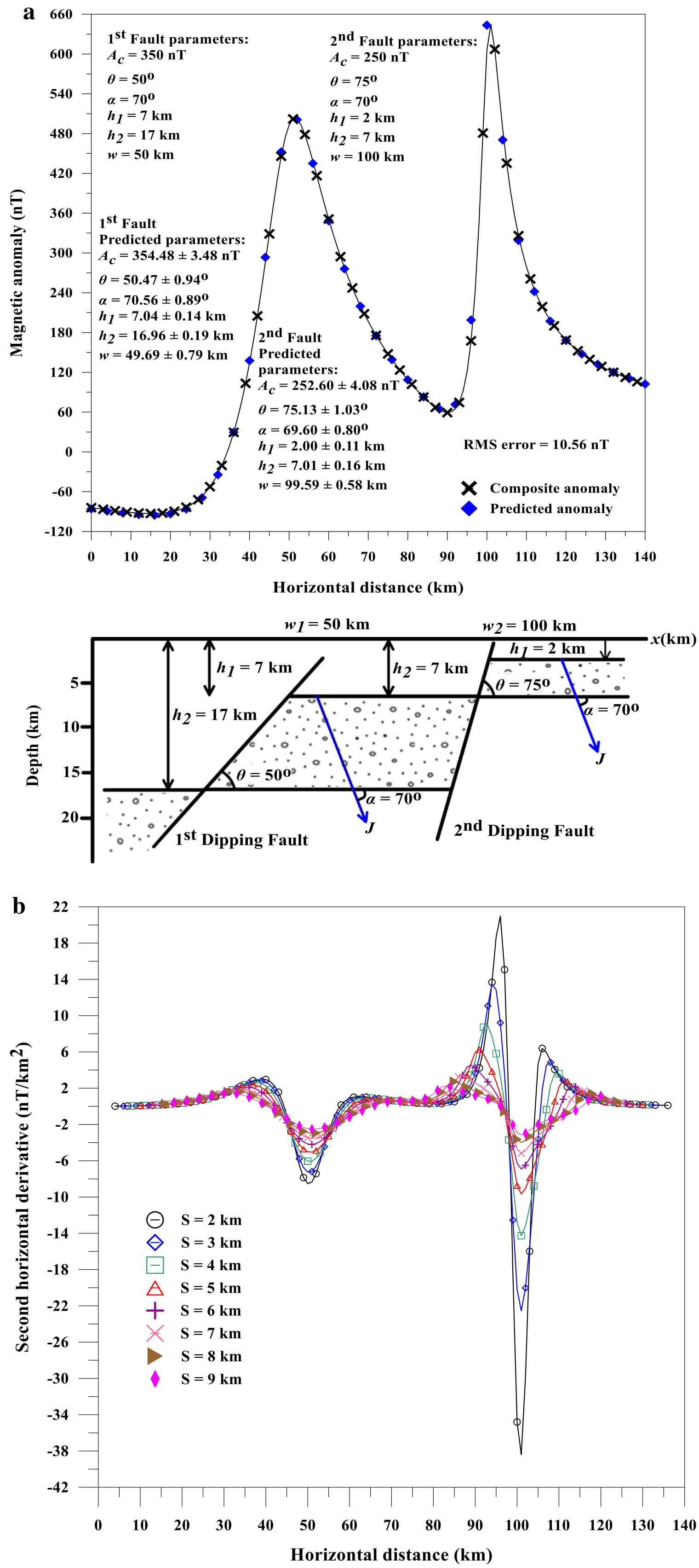

Table 3 Results of the global particle swarm optimization approach applied to second horizontal derivative anomalies for the magnetic anomaly profile (140 km) due to composite anomaly of dipping fault model ($A_c = 350$ nT, $\theta = 50°$, $\alpha = 70°$, $h_1 = 7$ km, $h_2 = 17$ km, and $w = 50$ km) and another dipping fault model ($A_c = 250$ nT, $\theta = 75°$, $\alpha = 70°$, $h_1 = 2$ km, $h_2 = 7$ km, and $w = 100$ km), without and with 20% noise

Model	Parameters	Used ranges	Using global particle swarm inversion for the magnetic derivative data										
			s = 2 km	s = 3 km	s = 4 km	s = 5 km	s = 6 km	s = 7 km	s = 8 km	s = 9 km	Average value ($G\mho$)	Error (%)	RMS error (nT)
Results (Noise free)													
Fault 1	A_c(nT)	100–800	355	352.47	354.84	357	359	352.38	357.17	348	354.48 ± 3.48	1.28	10.56
	θ(degree)	20–100	50.44	50.59	52.04	51	49.71	48.94	50	51.04	50.47 ± 0.94	0.94	
	α(degree)	30–100	69.51	69.16	70.57	71.45	70.42	71.75	71	70.62	70.56 ± 0.89	0.8	
	h_1(km)	3–11	7	7	7.1	7.2	7.2	6.9	6.8	7.1	7.04 ± 0.14	0.57	
	h_2(km)	10–22	17.1	17.2	16.9	16.8	17	16.7	16.8	17.2	16.96 ± 0.19	0.24	
	w (km)	40–60	49.47	49.56	48.93	48.82	49.72	49.34	51.07	50.64	49.69 ± 0.79	0.62	
Fault 2	A_c(nT)	50–700	253	247.17	250.39	254	247	254.81	256.42	258	252.60 ± 4.08	1.04	
	θ(degree)	40–110	76	75.8	74	76.12	76.28	74.20	73.81	74.83	75.13 ± 1.03	0.17	
	α(degree)	30–100	70.5	71	69	69.29	69	69.01	69	70	69.60 ± 0.80	0.57	
	h_1(km)	0.5–6	1.9	2	2.1	1.9	2	1.9	2.2	2	2.00 ± 0.11	0	
	h_2(km)	2–11	7.1	6.9	7.1	6.8	6.8	7.2	7	7.2	7.01 ± 0.16	0.14	
	w (km)	90–110	100.33	100.06	100.21	99.75	99.27	98.93	98.87	99.26	99.59 ± 0.58	0.46	
Results (using 20% noise)													
Fault 1	A_c(nT)	100–800	361	364	357.82	356.75	350.38	358.43	360.57	365	359.24 ± 4.60	2.64	18.49
	θ(degree)	20–100	53.48	46.93	52.91	53.31	49.11	52.07	48.72	51.10	50.95 ± 2.44	1.9	
	α(degree)	30–100	68.03	73.27	67.73	74.69	72.86	73	72.99	69.00	71.45 ± 2.73	2.07	
	h_1(km)	3–11	7.3	7.2	6.8	6.6	7.1	6.9	7.5	7.4	7.1 ± 0.31	1.43	
	h_2(km)	10–22	17.5	17.3	17.4	16.8	16.7	17.1	17.3	17.2	17.16 ± 0.28	0.94	
	w (km)	40–60	49.06	49.78	50.35	48.69	49.96	49.22	50.61	51.73	49.93 ± 0.98	0.14	
Fault 2	A_c(nT)	50–700	257.25	262.16	265.43	263	258.17	260.05	259.75	254.58	260.05 ± 3.45	4.02	
	θ(degree)	40–110	76.04	77.07	78.24	75.21	73.78	75	74.13	75.08	75.57 ± 1.49	0.76	
	α(degree)	30–100	74.41	72	73.17	70.09	71.10	69.21	68.56	71.14	71.21 ± 1.96	1.73	
	h_1(km)	0.5–6	1.8	1.7	1.8	2.2	1.7	2.1	2	1.9	1.9 ± 0.19	5	
	h_2(km)	2–11	7.2	6.6	7.4	7.1	7.2	7.3	6.8	7.3	7.11 ± 0.27	1.57	
	w (km)	90–110	99.38	100.7	99.43	101.33	99.04	98.91	99.72	99.63	99.77 ± 0.83	0.26	

Fig. 9 **a** The magnetic anomaly in Fig. 8a is contaminated with a 20% Gaussian noise and the predicted anomaly. **b** Second horizontal derivative anomalies are calculated from the noisy magnetic anomaly in Fig. 9a

a

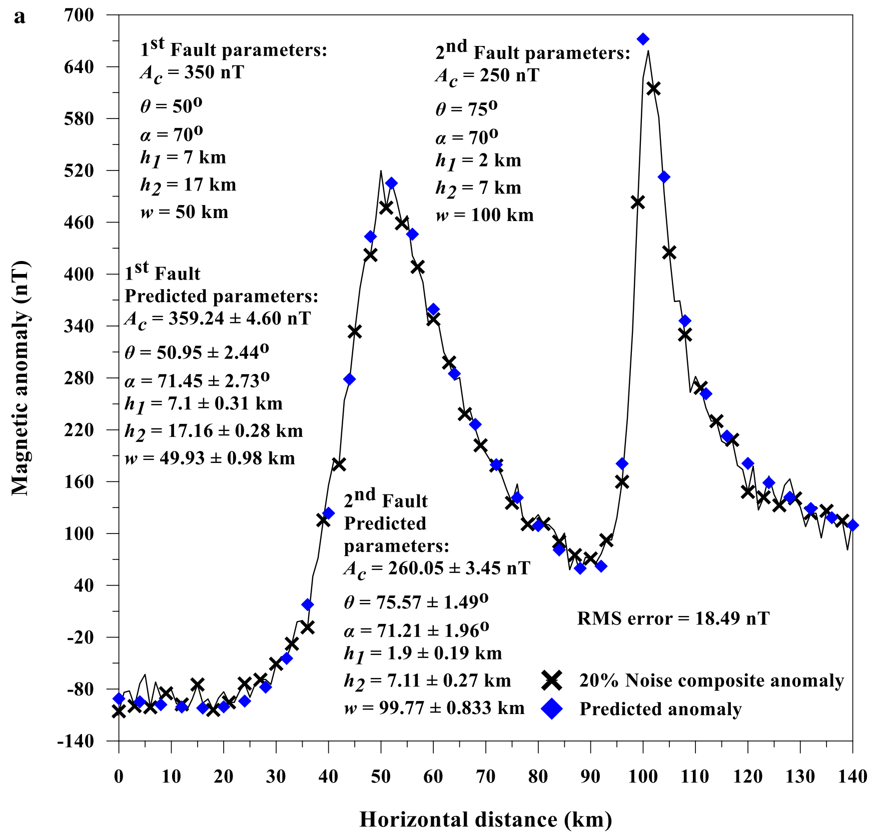

a

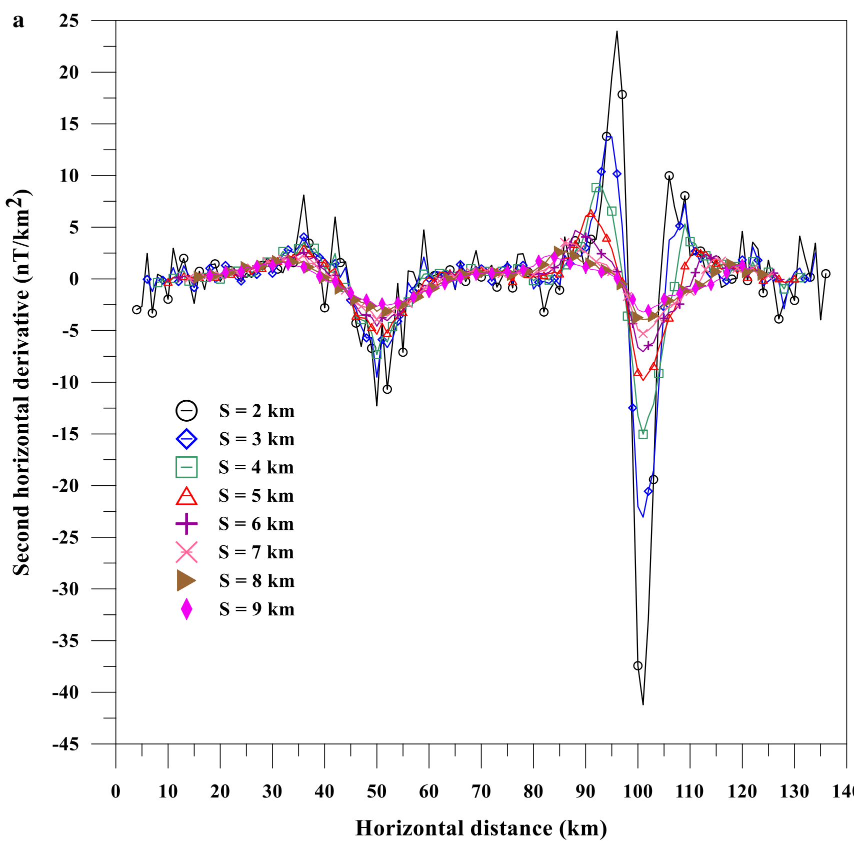

Fig. 10 **a** Geologic map of the Bihar area, India (modified after ▸ Prasad 1961); red rectangle indicates the study area (not to scale). **b** Observed and predicted magnetic anomaly profile for the East–West striking fault, Southwest of Dehri, Bihar zone, India. **c** Second horizontal derivative anomalies deliberated from the observed anomaly in Fig. 10b. **d** Convergence rate

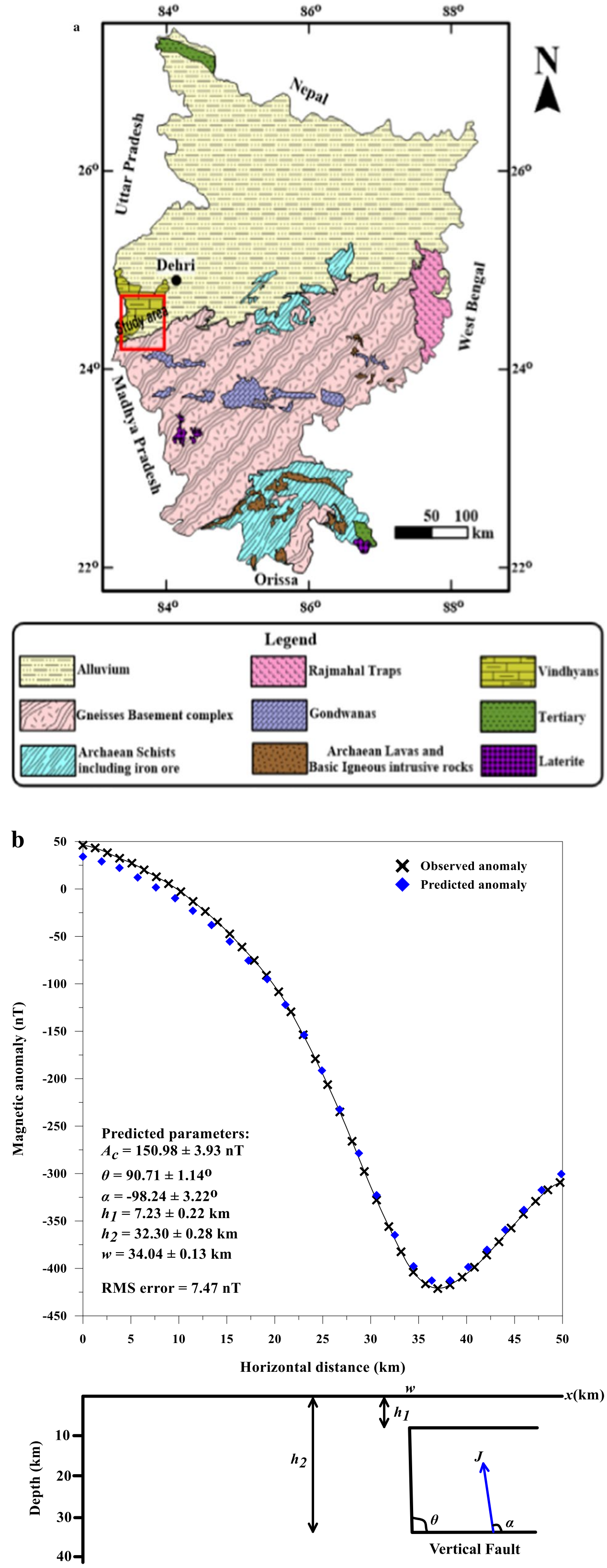

technique utilizing different graticule spacings (s = 2, 3, 4, 5, 6, 7, 8, and 9 km) (Fig. 3b). For estimating the different fault parameters, the particle swarm optimizer scheme was engaged to the calculated derivative anomalies using various ranges for the different parameters (Table 1). Table 1 explains the accuracy of the offered methodology through the errors (RMS) of valued parameters (A_c, θ, α, h_1, h_2, and w) which are 0%, and the RMS is 0 nT. The judgment between the predicted and the pure (noise-free) anomaly is revealed in Fig. 3a.

The efficacy of this approach in the presence of noise was assessed using the previous model infected with different Gaussian noise levels (15% and 20%).

Firstly, for a 15% noise anomaly (Fig. 4a), the noisy magnetic profile was subject to the second horizontal derivative technique, applying the same previous graticule spacings (Fig. 4b); the parameters were predicted by applying the particle swarm optimizer scheme (Table 1). Table 1 shows the predicted parameters (A_c = 303.88 ± 10.40 nT, θ = 69.36 ± 2.20°, α = 40.34 ± 2°, h_1 = 3.94 ± 0.23 km, h_2 = 10.06 ± 0.38 km, and w = 60.19 ± 0.35 km), where the errors of A_c, θ, α, h_1, h_2, and w are 1.29%, 0.91%, 0.85%, 1.5%, 0.6%, and 0.32%, respectively, while the RMS error is 8.91 nT. Figure 4a reveals the judgment among the predicted and noisy anomalies.

Secondly, for a 20% noise anomaly (Fig. 5a), the second horizontal derivative filter was exploited to the noisy anomaly profile with the previous graticule spacings (Fig. 5b). The particle swarm optimizer approach was employed for the derivative anomalies to predict the dipping fault parameters in case of a 20% noisy anomaly (Table 1). Table 1 presents the expected parameters (A_c = 309.82 ± 13.57 nT, θ = 70.78 ± 3.94°, α = 41.6 ± 2.3°, h_1 = 3.74 ± 0.19 km, h_2 = 10.33 ± 0.15 km, and w = 59.87 ± 0.68 km), where the errors of A_c, θ, α, h_1, h_2, and w are 3.27%, 1.11%, 4%, 6.5%, 3.3%, and 0.22%, respectively, while the RMS error is 21.71 nT.

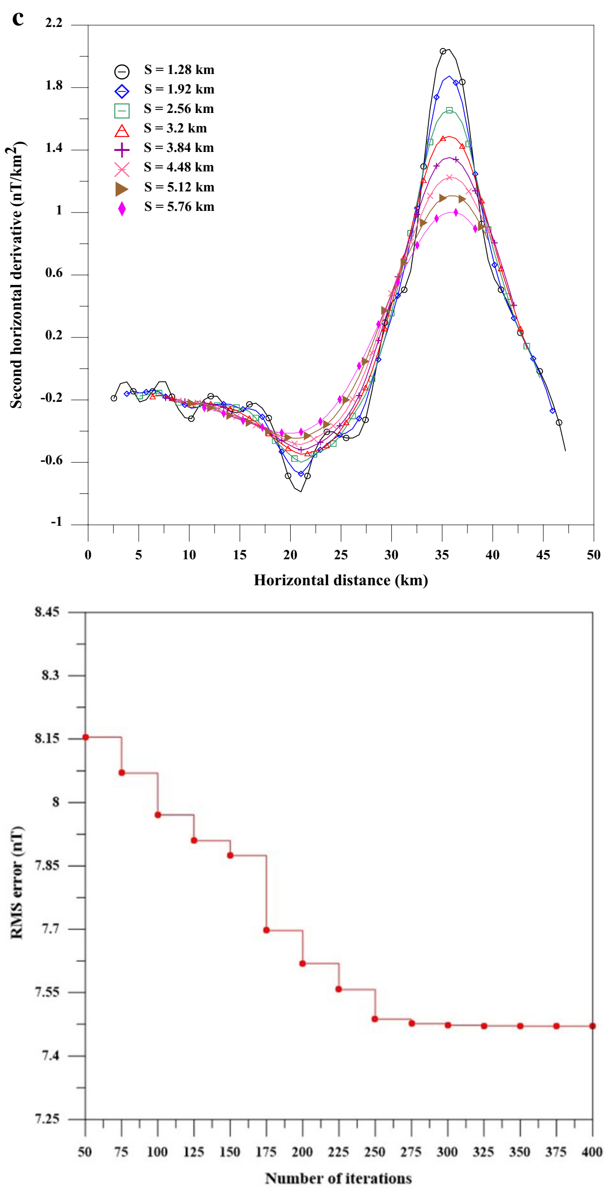

Fig. 10 (continued)

Figure 5a clarifies the contrast between the predicted and noisy anomalies.

Model II: Effect of regional background

A 120 km composite magnetic anomaly profile was produced. The profile was generated by a dipping fault (A_c = 450 nT, θ = 100°, α = 50°, h_1 = 5 km, h_2 = 16 km, and w = 75 km) superposed on a first-order regional background ($2x_i - 15$) (Fig. 6a).

The profile was filtered by applying the second horizontal derivative technique utilizing different graticule spacings (s = 2, 3, 4, 5, 6, 7, 8, and 9 km) (Fig. 6b). For appraising the different fault structure parameters, the global particle swarm optimizer was engaged with the calculated derivative anomalies applying various ranges for the parameters (Table 2). Table 2 indicates the predicted parameters (A_c, θ, α, h_1, h_2, and w) where the errors of A_c, θ, α, h_1, h_2, and w are 0%, and the RMS is 0 nT. The mismatch among the predicted and pure (noise-free) composite anomalies is mentioned in Fig. 6a.

The aforementioned model was tainted with 20% Gaussian noise (Fig. 7a). The second horizontal derivative scheme was utilized to this noisy data (Fig. 7b), and the parameters were predicted by applying the particle swarm optimizer procedure (Table 2). Table 2 indicates the predicted parameters (A_c = 460.52 ± 6.27 nT, θ = 102.46 ± 2.44°, α = 49.85 ± 2.35°, h_1 = 4.83 ± 0.33 km, h_2 = 16.11 ± 0.38 km, and w = 74.74 ± 0.44 km), where the errors of A_c, θ, α, h_1, h_2, and w are 2.34%, 2.46%, 0.3%, 3.4%, 0.69%, and 0.35%, respectively, while the RMS error is 21.04 nT. Figure 7a indicates the misfit among the predicted and noisy anomaly.

Model III: Multi-source

A composite magnetic profile of 140 km was produced. This profile was comprised of anomalies generated by two dipping faults (A_c = 350 nT, θ = 50°, α = 70°, h_1 = 7 km, h_2 = 17 km, and w = 50 km) and (A_c = 250 nT, θ = 75°, α = 70°, h_1 = 2 km, h_2 = 7 km, and w = 100 km) (Fig. 8a).

The composite anomaly profile was filtered by applying a second horizontal derivative technique utilizing different graticule spacings (s = 2, 3, 4, 5, 6, 7, 8, and 9 km) (Fig. 8b). The different fault parameters were predicted by a particle swarm optimizer scheme, which was applied to the calculated derivative anomalies utilizing various ranges for various parameters (Table 3). Table 3 reveals the predicted parameters: A_c = 354.48 ± 3.48 nT, θ = 50.47 ± 0.94°, α = 70.56 ± 0.89°, h_1 = 7.04 ± 0.14 km, h_2 = 16.96 ± 0.19 km, and w = 49.69 ± 0.79 km and the errors of A_c, θ, α, h_1, h_2, and w are 1.28%, 0.94%, 0.8%, 0.57%, 0.24%, and 0.62%, respectively, for the first fault, A_c = 252.60 ± 4.08 nT, θ = 75.13 ± 1.03°, α = 69.60 ± 0.80°, h_1 = 2.00 ± 0.11 km, h_2 = 7.01 ± 0.16 km, and w = 99.59 ± 0.58 km and the errors of A_c, θ, α, h_1, h_2, and w are 1.04%, 0.17%, 0.57%, 0%, 0.14%,

Table 4 Results of the global particle swarm optimization approach applied to second horizontal derivative anomalies for the magnetic anomaly profile of Dehri, Bihar area, India

Parameters	Used ranges	Using global particle swarm inversion for the magnetic derivative data									
		Results									
		s = 1.28 km	s = 1.92 km	s = 2.56 km	s = 3.2 km	s = 3.84 km	s = 4.48 km	s = 5.12 km	s = 5.76 km	Average value $(\overline{G})$	RMS error (nT)
A_c(nT)	20–350	145.29	149.51	148.31	151.76	153.40	147.97	154.38	157.24	150.98 ± 3.93	7.47
θ(degree)	30–170	91.17	91.02	89.47	92.41	90.03	88.97	91.00	91.58	90.71 ± 1.14	
α(degree)	−110 to 90	−95.97	−98.11	−96.51	−102.21	−104.07	−96.51	−94.87	−97.68	−98.24 ± 3.22	
h_1(km)	3–13	7.6	7.5	7.0	7.2	7.1	7.3	7.05	7.1	7.23 ± 0.22	
h_2(km)	15–40	32.6	32.3	31.89	32.4	31.97	32.7	32.2	32.32	32.30 ± 0.28	
w (km)	20–45	33.9	34.1	33.94	34.3	34.0	33.92	34.02	34.1	34.04 ± 0.13	

Table 5 A comparison between numerical solutions resulted from different methods for the magnetic anomaly profile of Dehri, Bihar area, India

Parameters	Methods		Present method
	Rama Rao et al. (1987) method	Radhakrishna Murthy et al. (2001) method	
A_c(nT)	–	–	150.98 ± 3.93
θ(degree)	–	90	90.71 ± 1.14
α(degree)	–	−97	−98.24 ± 3.22
h_1(km)	7.7	7.12	7.23 ± 0.22
h_2(km)	32.9	32.1	32.30 ± 0.28
w (km)	–	33	34.04 ± 0.13

and 0.46%, correspondingly, for the second fault and the RMS error of the multi-source model is 10.56 nT. The judgment between the predicted and pure (noise-free) composite anomalies is mentioned in Fig. 8a.

The former model was tainted with 20% Gaussian noise to assess the method's efficacy (Fig. 9a). The noisy magnetic profile was exposed to the second horizontal derivative technique employing similar graticule spacings (Fig. 9b). The different parameters for the two faults in the case of a noisy data were predicted by employing the particle swarm optimizer approach for derivative anomalies (Table 3). Table 3 indicates the predicted parameters in case of a noisy data: A_c = 359.24 ± 4.60 nT, θ = 50.95 ± 2.44°, α = 71.45 ± 2.73°, h_1 = 7.1 ± 0.31 km, h_2 = 17.16 ± 0.28 km, and w = 49.93 ± 0.98 km and the errors of A_c, θ, α, h_1, h_2, and w are 2.64%, 1.9%, 2.07%, 1.43%, 0.94%, and 0.14%, respectively, for the first fault. A_c = 260.05 ± 3.45 nT, θ = 75.57 ± 1.49°, α = 71.21 ± 1.96°, h_1 = 1.9 ± 0.19 km, h_2 = 7.11 ± 0.27 km, and w = 99.77 ± 0.83 km and the errors of A_c, θ, α, h_1, h_2, and w are 4.02%, 0.76%, 1.73%, 5%, 1.57%, and 0.26%, respectively, for the second fault and the RMS error of the multi-source noisy composite anomaly is 18.49 nT. The mismatch among the predicted and noisy composite anomalies is indicated in Fig. 9a.

Real datasets investigation

The efficacy and robustness of the proposed approach when employed with actual data from India, Australia, and Egypt were examined below as follows:

Magnetic anomaly from Dehri, Bihar Area, India

The geology of the Bihar area, India, is composed of different units which are (from recent to Archean) (Karan 1953; Prasad 1961); Quaternary alluvium deposits, which include

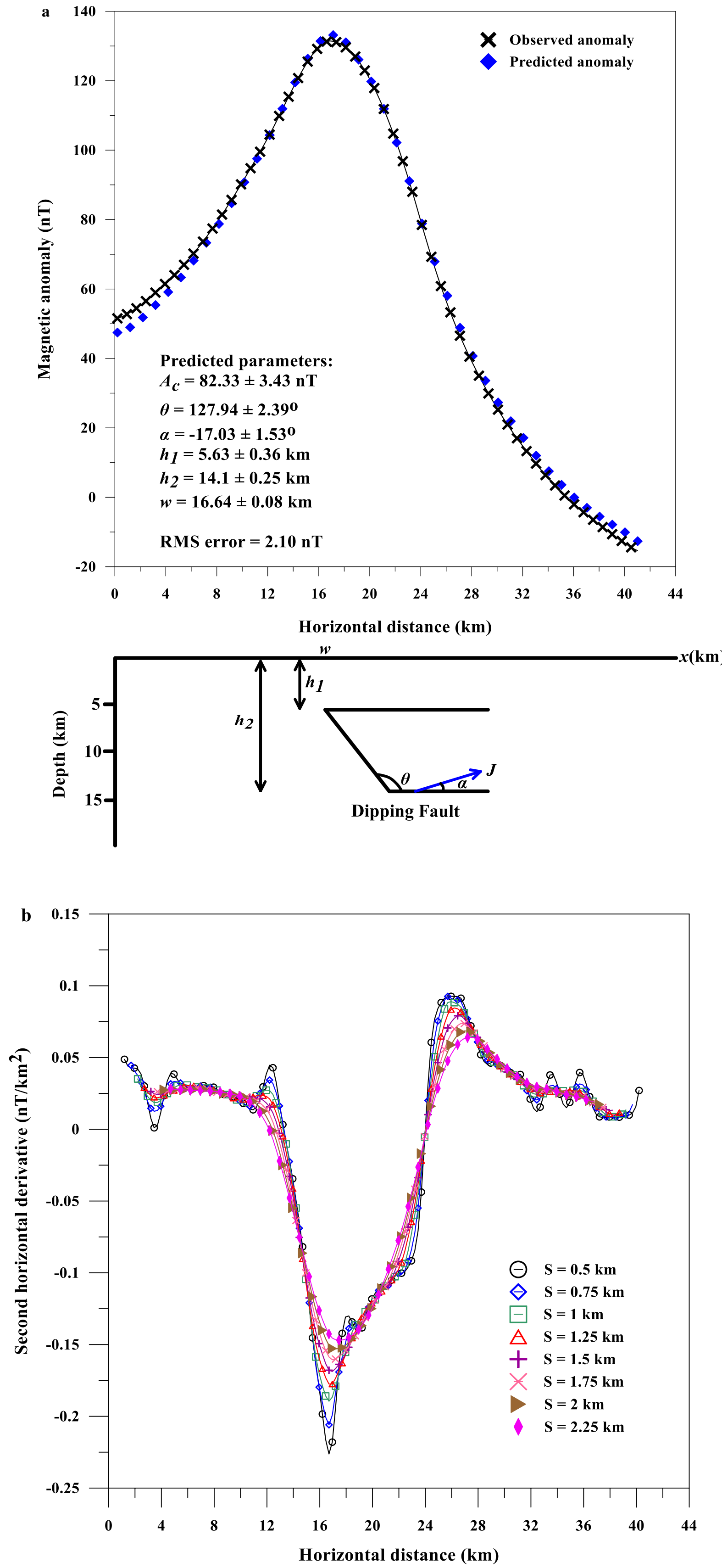

Fig. 11 **a** Observed and predicted magnetic anomaly profile for the north–south striking fault, Western edge of Perth basin, Australia. **b** Second horizontal derivative anomalies deliberated from the observed anomaly in Fig. 11a. **c** Convergence rate

Fig. 11 (continued)

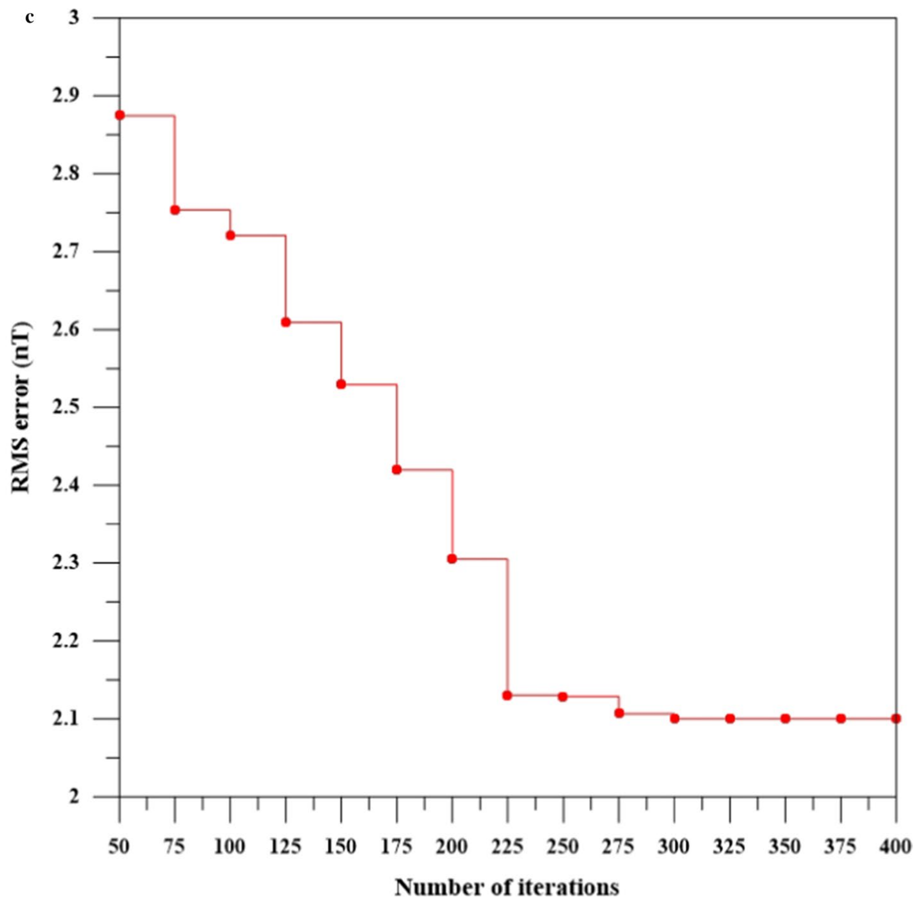

various grades of clay, silt, sand, and gravel; Laterite, which is rich in aluminum and iron; a Tertiary unit, which includes sandstones and claystones; the Mesozoic layered volcanic unit named the Rajmahal Traps; the Paleozoic Vindhyans Supergroup which is comprised of limestone, sandstone, and shale; the Archaean lavas and basic igneous intrusive rocks; the Archean schists which include an iron ore series; and the gneiss basement complex (Prasad 1961) (Fig. 10a).

The magnetic anomaly profile data were acquired southwest of Dehri, Bihar zone, India. This anomaly was generated by an east–west striking fault (Rama Rao et al. 1987; Murthy et al. 2001). The magnetic profile length equal to 50 km was digitized at 0.64 km (Fig. 10b). The second horizontal derivative technique processed the profile using different graticule spacings (s = 1.28, 1.92, 2.56, 3.2, 3.84, 4.48, 5.12, and 5.76 km) (Fig. 10c). To estimate the different fault parameters (A_c, θ, α, h_1, h_2, and w), the particle swarm optimizer algorithm was engaged to derivative anomalies using various ranges (Table 4), the predicted parameters are: A_c = 150.98 ± 3.93 nT, θ = 90.71 ± 1.14°, α = − 98.24 ± 3.22°, h_1 = 7.23 ± 0.22 km, h_2 = 32.30 ± 0.28 km, and w = 34.04 ± 0.13, and the RMS error is 7.47 nT. The comparison among observed and predicted anomalies is displayed in Fig. 10a. Moreover, the convergence rate is indicated in Fig. 10d. Table 5 shows the correlation between the parameters estimated by the suggested process and those estimated by other methods published in the literature.

Magnetic anomaly from Perth Basin, Australia

Perth Basin was initiated by the intercontinental rift on the eastern side of Gondwana and advanced, through the separation of Greater India from Australia, into an inactive edge alongside southwestern Australia (Harris 1994; Ali and Aitchison 2014; Olierook et al. 2015). The basin is subdivided into at least fifteen sub-basins, filled with sedimentary layers ranging in age from the Permian to the Recent. The sediment rocks are mainly fluviatile and trivial marine

Table 6 Results of the global particle swarm optimization approach applied to second horizontal derivative anomalies for the magnetic anomaly profile of Perth Basin, Australia

Parameters	Used ranges	Using global particle swarm inversion for the magnetic derivative data									
		Results									
		s = 0.5 km	s = 0.75 km	s = 1 km	s = 1.25 km	s = 1.5 km	s = 1.75 km	s = 2 km	s = 2.25 km	Average value ($G\mathcal{D}$)	RMS error (nT)
A_c(nT)	10–300	82.41	85.56	76.63	83.91	81.72	84.11	86.24	78.07	82.33 ± 3.43	2.10
θ(degree)	40–170	128.05	125.42	129.81	131.53	130.02	127.81	126.0	124.91	127.94 ± 2.39	
α(degree)	− 70 to 90	− 17.0	− 14.58	− 16.12	− 18.34	− 15.71	− 19.29	− 17.21	− 18.0	− 17.03 ± 1.53	
h_1(km)	2–13	5.4	5.2	5.5	5.3	6.1	5.7	6.2	5.6	5.63 ± 0.36	
h_2(km)	5–30	14.1	14.3	13.7	14.3	14.2	13.8	14.4	14	14.1 ± 0.25	
w (km)	10–30	16.8	16.71	16.54	16.62	16.58	16.59	16.64	16.67	16.64 ± 0.08	

Table 7 A comparison between numerical solutions resulted from different methods for the magnetic anomaly profile of Perth Basin, Australia

Parameters	Methods				
	Qureshi & Nalaye (1978) method	Radhakrishna Murthy et al. (2001) method	Ekinci et al. (2019) method		Present method
			DE method	PSO method	
A_c(nT)	–	–	–	–	82.33 ± 3.43
θ(degree)	–	97	141.13	142.10	127.94 ± 2.39
α(degree)	–	− 20	− 14.93	− 14.04	− 17.03 ± 1.53
h_1(km)	6.3–6.85	6.21	5.10	5.34	5.63 ± 0.36
h_2(km)	15.55–16.5	15.07	13.76	13.32	14.1 ± 0.25
w (km)	–	18.5	17.16	17.13	16.64 ± 0.08

intrusions (Olierook et al. 2015). The basin's eastern edge is noticeably designed by a Darling Fault, which isolates it from the Precambrian rock bearing Yilgarn Craton; the northern and southern edges are bordered by the Northampton block and the Leeuwin block, respectively. Both blocks are Precambrian in age (Qureshi and Nalaye 1978; Olierook et al. 2015).

A magnetic anomaly profile was acquired across the western edge of Perth Basin. This residual anomaly is generated by a deeper north–south striking fault (Qureshi and Nalaye 1978; Murthy et al. 2001; Ekinci et al. 2019). The magnetic profile length was 41 km and digitized at 0.25 km (Fig. 11a). The profile was filtered using the second horizontal derivative technique using different graticule spacings (s = 0.5, 0.75, 1, 1.25, 1.5, 1.75, 2, and 2.25 km) (Fig. 11b). To estimate the different fault parameters (A_c, θ, α, h_1, h_2, and w), the particle swarm optimizer scheme was engaged with derivative anomalies utilizing various ranges (Table 6). The predicted parameters are: A_c = 82.33 ± 3.43 nT, θ = 127.94 ± 2.39°, α = − 17.03 ± 1.53°, h_1 = 5.63 ± 0.36 km, h_2 = 14.1 ± 0.25 km, and w = 16.64 ± 0.08, and the RMS error is 2.10 nT. Furthermore, the convergence rate is represented in Fig. 11c. The close relationship between observed and predicted anomalies is displayed in Fig. 11a. Table 7 shows the correlation between the parameters estimated by this method and those estimated by other published methods, and the depths to the top and the bottom of this fault are estimated by Qureshi and Nalaye (1978) using master curves and analytical methods. (Murthy et al. 2001) by using a damped least-square inversion method estimated the depths to the top and the bottom of this fault, the fault angle, and the effective magnetization vector dip angle. (Ekinci et al. 2019) estimated the depths to the top and the bottom of this fault, the fault angle, and the effective magnetization vector dip angle.

Magnetic anomaly from the Central Eastern Desert, Egypt

Figure 12a shows the study area "Central Eastern Desert," which is in the middle part of Eastern Desert, Egypt, and characterized by a dominant NW–SE sinistral shear zone of the Najd Fault System that represents one of the larger Neoproterozoic shear zones on the Earth (Stern 1985). The area is characterized by dome structures, which are fabricated from medium to high grade gneisses–migmatites (core) and the upper part of volcanogenic metagraywackes, metamudstones, and ophiolitic (Pan-African Nappe complex) (Fowler et al. 2007; Hamimi et al. 2019).

Figure 12b shows a profile A–Á for the land magnetic data acquired across the study area and was digitized with intervals of 0.5 km (taken from Rabeh 2009; Fig. 12). This magnetic profile was filtered applying the second horizontal derivative technique using different graticule spacings (s = 1.0, 1.5, 2.0, 2.5, 3.0, 3.5, 4.0, and 4.5 km) (Fig. 12c). The fault parameters (A_c, θ, α, h_1, h_2, and w) were calculated by applying particle swarm optimization algorithm to the calculated gradient anomalies (Table 8). Table 8 shows the predicted parameters, which are A_c = −9.84 ± 0.62 nT, θ = 42.92 ± 1.14°, α = 30.85 ± 0.62°, h_1 = 0.78 ± 0.02 km, h_2 = 1.76 ± 0.03 km, and w = 35.64 ± 0.02, and the RMS error is 0.43 nT. Moreover, the convergence rate is exposed in Fig. 12d. The match among observed and predicted anomalies is displayed in Fig. 12b. These results show a satisfactory correlation with the geologic cross section after said (1990), the 2.5D magnetic model along the aeromagnetic profile (Rabeh 2009; Fig. 12).

From the above three field examples, we can conclude that the method can be used effectively for different types of faults as in the first field example (Dehri, Bihar Area, India), and the fault is vertical (θ = 90.71 ± 1.14°), while

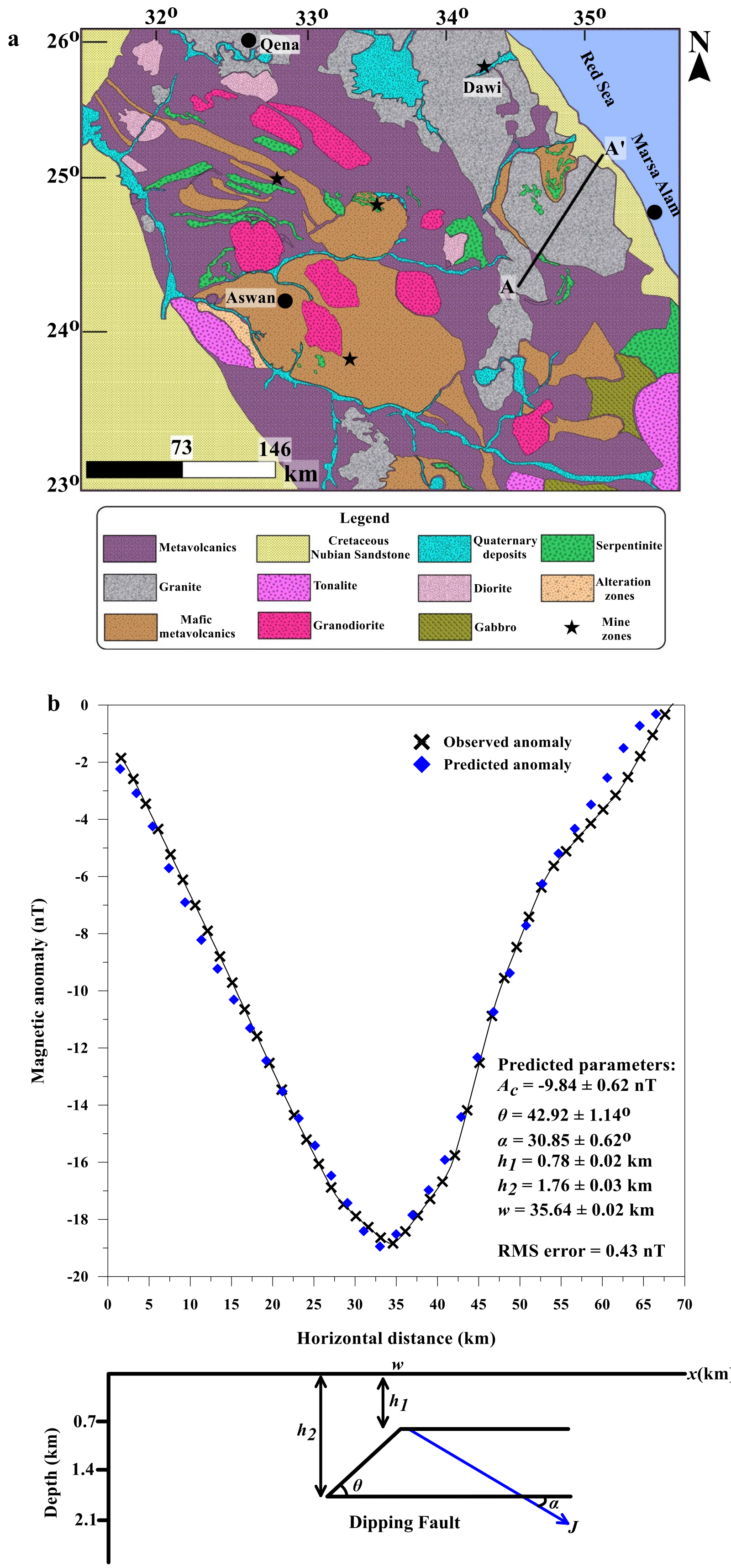

Fig. 12 **a** Geological map of the central Eastern Desert, Egypt (modified after Conoco and Egyptian General Petroleum Corporation 1987; Rabeh 2009), showing the location of the magnetic profile, A–Á. **b** The observed and the predicted magnetic anomaly profile f A–Á, Central Eastern Desert, Egypt. **c** Second horizontal derivative anomalies deliberated from the observed anomaly in Fig. 12a. **d** Convergence rate

Fig. 12 (continued)

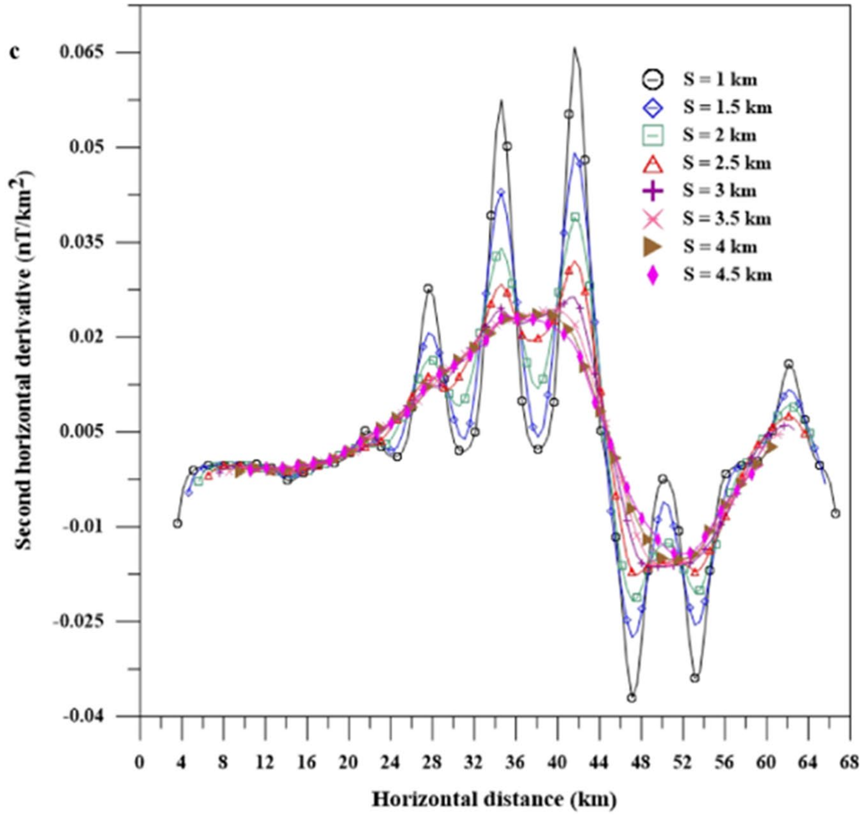

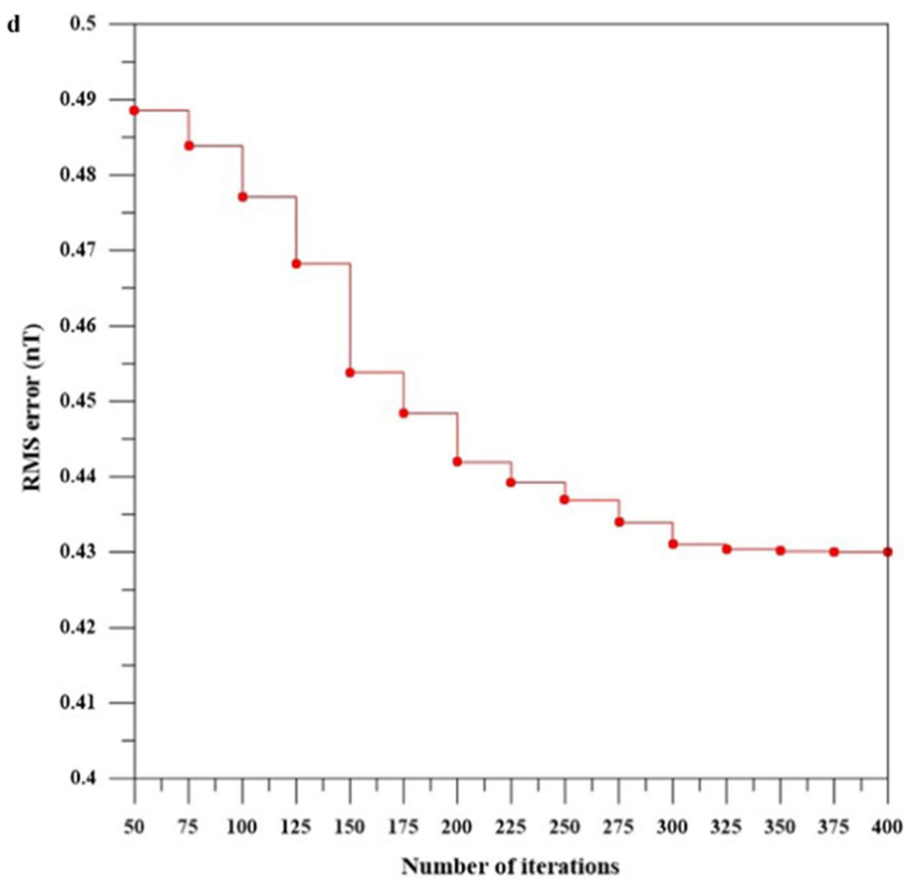

Table 8 Results of the global particle swarm optimization approach applied to second horizontal derivative anomalies for the magnetic anomaly profile A–Á of the Central Eastern Desert, Egypt

Parameters	Used ranges	Using global particle swarm inversion for the magnetic derivative data									
		Results									
		s = 1 km	s = 1.5 km	s = 2 km	s = 2.5 km	s = 3 km	s = 3.5 km	s = 4 km	s = 4.5 km	Average value ($\bar{G}$)	RMS error (nT)
A_c(nT)	−50 to 50	−11.21	−12.57	−8.79	−10.27	−9.41	−10.73	−9.57	−10.18	−9.84 ± 0.62	0.43
θ(deg)	20–100	41.35	41.61	42.17	42.83	43.19	44.21	43.55	44.42	42.92 ± 1.14	
α(deg)	10–90	31.51	31.36	30.41	30.15	31.76	30.86	30.22	30.54	30.85 ± 0.62	
h_1(km)	0.1–2	0.78	0.76	0.79	0.81	0.77	0.80	0.74	0.79	0.78 ± 0.02	
h_2(km)	2.2–5	1.73	1.75	1.74	1.78	1.79	1.76	1.78	1.77	1.76 ± 0.03	
w (km)	20–40	35.62	35.61	35.64	35.63	35.65	35.62	35.63	35.64	35.64 ± 0.02	

the faults in the second (Perth Basin, Australia) and the third (Central Eastern Desert, Egypt) field examples are dipping as $\theta = 127.94 \pm 2.39°$ and $\theta = 42.92 \pm 1.14°$ for the second and third field example, respectively. The third field example represents the shallowest fault as the depth is 0.78 ± 0.02 km, while in the second field example, the depth is 5.63 ± 0.36 km, and in the first one the depth is 7.23 ± 0.22 km; also, the length of the fault in the third field example is the shortest which is about 0.98 km, while in the second field example, the length is about 8.47 km, and in the first one which represents the longest is about 25.07 km.

Conclusions

An extended combination of applying the particle swarm optimizer and second horizontal derivative schemes to interpret and investigate the magnetic data generated by dipping and vertical faults was presented. This method can be effectively applied to geophysical exploration data (e.g., mining), and fault characterization data. Besides, it can estimate the multiple fault parameters (amplitude coefficient (A_c), fault angle (θ), effective magnetization vector dip angle (α), depth to the upper side of the fault (h_1), depth to the lower side of the fault (h_2), and the fault origin (w)). Moreover, it completely removes the regional magnetic background. The suggested approach's applicability and efficacy were verified utilizing six different data sets, three synthetic and three real examples (from India, Australia, and Egypt, respectively). The models generated for the actual data sets correlated well with the faults described in published literature.

Acknowledgements Authors would like to thank Prof. Dr. Eleftheria E. Papadimitriou, Editor-in-Chief, Prof. Dr. Ivana Vasiljevic, Associate Editor, and the two reviewers for their keen interest, valuable comments on the manuscript, and improvements to this work.

Funding Open access funding provided by The Science, Technology & Innovation Funding Authority (STDF) in cooperation with The Egyptian Knowledge Bank (EKB).

Declarations

Conflict of interest The authors declare that they have no known competing interests.

References

Abdelrahman EM, Essa KS (2005) Magnetic interpretation using a least-squares, depth-shape curves method. Geophysics 70:L23–L30

Abdelrahman EM, EL-Araby HM, EL-Araby TM, Essa KS (2003) A least-squares minimization approach to depth determination from magnetic data. Pure Appl Geophys 160:1259–1271

Abdelrahman EM, Abo-Ezz ER, Essa KS, El-Araby TM, Soliman KS (2007) A new least-squares minimization approach to depth and shape determination from magnetic data. Geophys Prospect 55:433–446

Abdullahi M, Kumar R (2020) Curie depth estimated from high-resolution aeromagnetic data of parts of lower and middle Benue trough (Nigeria). Acta Geod Geophys 55:627–643

Abraham EM, Lawal KM, Ekwe AC, Alile O, Murana KA, Lawal AA (2014) Spectral analysis of aeromagnetic data for geothermal energy investigation of Ikogosi Warm Spring-Ekiti State, southwestern Nigeria. Geotherm Energy 2:6

Abubakar R, Muxworthy AR, Sephton MA, Southern P, Watson JS, Fraser AJ (2015) Formation of magnetic minerals at hydrocarbon-generation conditions. Mar Pet Geol 68:509–519

Agarwal BNP, Srivastava S (2010) A FORTRAN program to implement the method of finite elements to compute regional and residual anomalies from gravity data. Comput Geosci 36:848–852

Ai H, Essa KS, Ekinci YL, Balkaya Ç, Li H, Géraud Y (2022) Magnetic anomaly inversion through the novel barnacles mating optimization algorithm. Sci Rep 12:22578

Akinlalu AA, Adelusi AO, Olayanju GM, Adiat KN, Omosuyi GO (2018) Aeromagnetic mapping of basement structures and mineralization characterisation of Ilesa Schist Belt, Southwestern Nigeria. J Afr Earth Sci 138:383–391

Ali JR, Aitchison JC (2014) Greater India's northern margin prior to its collision with Asia. Basin Res 26:73–84

An Z, Di Q (2016) Investigation of geological structures with a view to HLRW disposal, as revealed through 3D inversion of aeromagnetic and gravity data and the results of CSAMT exploration. J Appl Geophys 135:204–211

Araffa SAS, Bedair S (2021) Application of land magnetic and geoelectrical techniques for delineating groundwater aquifer: case study in East Oweinat, Western Desert. Egypt Nat Resour Res 30:4219–4233

Aydin I (2008) Estimation of the location and depth parameters of 2D magnetic sources using analytical signals. J Geophys Eng 5:281–289

Balkaya C, Göktürkler G, Erhan Z, Ekinci YL (2012) Exploration for a cave by magnetic and electrical resistivity surveys: Ayvacık Sinkhole example, Bozdağ, İzmir (western Turkey). Geophysics 77:B135–B146

Biswas A (2016) Interpretation of gravity and magnetic anomaly over thin sheet-type structure using very fast simulated annealing global optimization technique. Model Earth Syst Environ 2:30

Biswas A (2018) Inversion of source parameters from magnetic anomalies for mineral/ore deposits exploration using global optimization technique and analysis of uncertainty. Nat Resour Res 27:77–107

Biswas A, Acharya T (2016) A very fast simulated annealing (VFSA) method for inversion of magnetic anomaly over semi-infinite vertical rod-type structure. Model Earth Syst Environ 2:198

Currenti G, Del Negro C, Fortuna L, Ganci G (2007) Integrated inversion of ground deformation and magnetic data at Etna volcano using a genetic algorithm technique. Ann Geophys 50:21–30

Deng H, Hu X, Cai H et al (2022) 3D inversion of magnetic gradient tensor data based on convolutional neural networks. Minerals 12:566

Dewangan P, Ramprasad T, Ramana MV, Desa M, Shailaja B (2007) Automatic interpretation of magnetic data using Euler deconvolution with nonlinear background. Pure Appl Geophys 164:2359–2372

Eberhart R, Kennedy J (1995) A new optimizer using particle swarm theory. In: MHS'95. Proceedings of the sixth international symposium on micro machine and human science, pp 39–43

Ekinci YL, Balkaya Ç, Göktürkler G (2019) Parameter estimations from gravity and magnetic anomalies due to deep-seated faults: differential evolution versus particle swarm optimization. Turk J Earth Sci 28:860–881

Elhussein M (2021) A novel approach to self-potential data interpretation in support of mineral resource development. Nat Resour Res 30:97–127

Elhussein M, Shokry M (2020) Use of the airborne magnetic data for edge basalt detection in Qaret Had El Bahr area, Northeastern Bahariya Oasis. Egypt Bull Eng Geol Environ 79:4483–4499

Essa KS (2021) Evaluation of the parameters of fault-like geologic structure from the gravity anomalies applying the particle swarm. Environ Earth Sci 80:489

Essa KS, Diab ZE (2022a) An automatic inversion approach for magnetic data applying the global bat optimization algorithm (GBOA): application to ore deposits and basement rock intrusion. Geomech Geophys Geo-Energ Geo-Resour 8:185

Essa KS, Diab ZE (2022b) Magnetic data interpretation for 2D dikes by the metaheuristic bat algorithm: sustainable development cases. Sci Rep 12:14206

Essa KS, Elhussein M (2017) A new approach for the interpretation of magnetic data by a 2-D dipping dike. J Appl Geophys 136:431–443

Essa KS, Elhussein M (2018) PSO (particle swarm optimization) for interpretation of magnetic anomalies caused by simple geometrical structures. Pure Appl Geophys 175:3539–3553

Essa KS, Elhussein M (2019) Magnetic interpretation utilizing a new inverse algorithm for assessing the parameters of buried inclined dike-like geologic structure. Acta Geophys 67:533–544

Essa KS, Elhussein M (2020) Interpretation of magnetic data through particle swarm optimization: mineral exploration cases studies. Nat Resour Res 29:521–537

Essa KS, Géraud Y (2020) Parameters estimation from the gravity anomaly caused by the two-dimensional horizontal thin sheet applying the global particle swarm algorithm. J Pet Sci Eng 193:107421

Essa KS, Nady AG, Mostafa MS, Elhussein M (2018) Implementation of potential field data to depict the structural lineaments of the Sinai Peninsula. Egypt J Afr Earth Sci 147:43–53

Essa KS, Géraud Y, Diraison M (2021) Fault parameters assessment from the gravity data profiles using the global particle swarm optimization. J Pet Sci Eng 207:109129

Essa KS, Munschy M, Youssef MAS et al (2022) Aeromagnetic and radiometric data interpretation to delineate the structural elements and probable precambrian mineralization zones: a case study. Egypt Min Metall Explor 39:2461–2475

Essa KS, Abo-Ezz ER, Géraud Y, Diraison M (2023) A successful inversion of magnetic anomalies related to 2D dyke-models by a particle swarm scheme. J Earth Syst Sci 132:65

Fowler A, Khamees H, Dowidar H (2007) El Sibai gneissic complex, Central Eastern Desert, Egypt: folded nappes and syn-kinematic gneissic granitoid sheets – not a core complex. J Afr Earth Sci 49:119–135

Gay P (1963) Standard curves for interpretation of magnetic anomalies over long tabular bodies. Geophysics 28:161–200
Gerard-Little PA, Rogers MB, Jordan KA (2012) Understanding the built environment at the Seneca Iroquois White Springs Site using large-scale, multi-instrument archaeogeophysical surveys. J Archaeol Sci 39:2042–2048
Ghanati R, Ghari H, Fatehi M (2017) Regularized nonlinear inversion of magnetic anomalies of simple geometric models using Occam's method: an application to the Morvarid iron-apatite deposit in Iran. Acta Geod Geophys 52:555–580
Grant S, Martin L (1966) Interpretation of aeromagnetic anomalies by the use of characteristic curves. Geophysics 31:135–148
Gudmundsson G (1966) Interpretation of one-dimensional magnetic anomalies by use of the Fourier-transform. Geophys J R Astr Soc 12:87–97
Gupta OP (1988) A Fourier transform minimization technique for interpreting magnetic anomalies of some two-dimensional bodies. Can J Explor Geophys 24:179–184
Hajian A, Zomorrodian H, Styles P (2012) Simultaneous estimation of shape factor and depth of subsurface cavities from residual gravity anomalies using feed-forward back-propagation neural networks. Acta Geophys 60:1043–1075
Hamimi Z, Abd El-Wahed MA, Gahlan HA, Kamh SZ (2019) Tectonics of the Eastern Desert of Egypt: key to understanding the Neoproterozoic evolution of the Arabian-Nubian Shield (East African Orogen). In: Bendaoud A, Hamimi Z, Hamoudi M, Djemai S, Zoheir B (eds) Geology of the Arab World—an overview, Springer Geology. Springer Geology, pp 1–81
Hansen RO (2005) 3D multiple-source Werner deconvolution for magnetic data. Geophysics 70:L45–L51
Harris LB (1994) Structural and tectonic synthesis for the Perth Basin, Western Australia. J Pet Geol 17:129–156
Hosseini SH, Habibian Dehkordi B, Abedi M (2021) Implications for a geothermal reservoir at Abgarm, Mahallat, Iran: Magnetic and Magnetotelluric Signatures. Nat Resour Res 30:59–272
Hutchison RD (1958) Magnetic analysis by logarithmic curves. Geophysics 23:749–767
Innocent AJ, Chidubem EO, Chibuzor NA (2019) Analysis of aeromagnetic anomalies and structural lineaments for mineral and hydrocarbon exploration in Ikom and its environs southeastern Nigeria. J Afr Earth Sci 151:274–285
Ivakhnenkoa OP, Abirova R, Logvinenkoc A (2015) New method for characterisation of petroleum reservoir fluid mineral deposits using magnetic analysis. Energy Proced 76:454–462
Kaftan I (2017) Interpretation of magnetic anomalies using a genetic algorithm. Acta Geophys 65:627–634
Karan PP (1953) Economic regions of Chota Nagpur, Bihar, India. Econ Geogr 29:216–250
Kushwaha N, Pant M, Kant S, Jain VK (2018) Magnetic optimization algorithm for data clustering. Pattern Recognit Lett 115:59–65
Li X (2003) On the use of different methods for estimating magnetic depth. Lead Edge 22:1090–1101
Linford N, Linford P, Payne A (2019) Advanced magnetic prospecting for archaeology with a vehicle-towed array of cesium magnetometers. In: Persico R, Piro S, Linford N (eds) Innovation in near-surface geophysics
Liu S, Liang M, Hu X (2017) Particle swarm optimization inversion of magnetic data: field examples from iron ore deposits in China. Geophysics 83:1JA-Z18
Liu Y, Xia Q, Cheng Q (2021) Aeromagnetic and geochemical signatures in the Chinese Western Tianshan: implications for tectonic setting and mineral exploration. Nat Resour Res 30:3165–3195
Mandal A, Mohanty WK, Sharma SP, Biswas A, Sen J, Bhatt AK (2015) Geophysical signatures of uranium mineralization and its subsurface validation at Beldih, Purulia District, West Bengal, India: a case study. Geophys Prospect 63:713–726
Mehanee S, Essa KS, Diab ZE (2021) Magnetic data interpretation using a new R-parameter imaging method with application to mineral exploration. Nat Resour Res 30:77–95
Melo AT, Li Y, Hitzman M (2020) Is there hidden potential in Carajás? Insights through the geophysical signature of Cristalino deposit. Ore Geol Rev 126:103735
Miller HG, Singh V (1994) Potential field tilt—a new concept for location of potential field sources. J Appl Geophys 32:213–217
Montesinos FG, Blanco-Monegro I, Arnoso J (2016) Three-dimensional inverse modelling of magnetic anomaly sources based on a genetic algorithm. Phys Earth Planet Int 253:74–87
Murthy IVR, Swamy KV, Rao SJ (2001) Automatic inversion of magnetic anomalies of faults. Comput Geosci 27:315–325
Nabighian MN (1972) The analytic signal of two-dimensional bodies with polygonal cross-section: Its properties and use for automated interpretation. Geophysics 37:507–517
Niederleithinger E, Weller A, Lewis R (2012) Evaluation of geophysical techniques for dike inspection. J Environ Eng Geophys 17:185–195
Olierook HKH, Timms NE, Wellmann JF, Corbel S, Wilkes PG (2015) 3D structural and stratigraphic model of the Perth Basin, Western Australia: implications for sub-basin evolution. Aust J Earth Sci 62:447–467
Olurin OT, Ganiyu SA, Hammed OS, Aluko TJ (2017) Interpretation of aeromagnetic data over Abeokuta and its environs, Southwest Nigeria, using spectral analysis (Fourier transform technique). Mater Geoenviron 63:199–212
Pace F, Santilano A, Godio A (2021) A review of geophysical modeling based on particle swarm optimization. Surv Geophys 42:505–549. https://doi.org/10.1007/s10712-021-09638-4
Pawlowski RS (1994) Green's equivalent-layer concept in gravity band-pass filter design. Geophysics 59:69–76
Pham LT, Oksum E, Do TD (2019) Edge enhancement of potential field data using the logistic function and the total horizontal gradient. Acta Geod Geophys 54:143–155
Prasad SD (1961) Census of India 1961. Central Government Publications, IV
Qureshi IP, Nalaye AM (1978) A method for direct interpretation of magnetic anomalies caused by 2-d vertical faults. Geophysics 43:179–188
Rabeh T (2009) Prospecting for the ferromagnetic mineral accumulations using the magnetic method at the Eastern Desert. Egypt J Geophys Eng 6:401–411
Rama Rao Ch, Veeraswamy K, Sarma MRL, Baskara Rao DS (1987) Interpretation of magnetic anomalies due to infinite dyke and vertical steps using relation figures. Geophys Res Bull 25:178–183
Reynolds JM (2011) An introduction to applied and environmental geophysics. Wiley, New York
Said R (1990) The geology of Egypt. Elsevier, Amsterdam, New York
Salem A (2005) Interpretation of magnetic data using analytic signal derivatives. Geophys Prospect 53:75–82
Saunders DF, Burson KR, Thompson CK (1991) Observed relation of soil magnetic susceptibility and soil gas hydrocarbon analyses to subsurface hydrocarbon accumulations. AAPG Bull 75:389–408
Scollar I, Weidner B, Segeth K (1986) Display of archaeological magnetic data. Geophysics 51:623–633
Shirani S, Nejati Kalateh A, Noorollahi Y (2020) Curie point depth estimations for Northwest Iran through spectral analysis of aeromagnetic data for geothermal resources exploration. Nat Resour Res 29:2307–2332
Singh A, Biswas A (2016) Application of global particle swarm optimization for inversion of residual gravity anomalies over

geological bodies with idealized geometries. Nat Resour Res 25:297–314

Stagg HMJ, Wilcox JB, Needham DJL (1989) Werner deconvolution of magnetic data: Theoretical models and application to the Great Australian Bight. Aust J Earth Sci 36:109–122

Stern RJ (1985) The Najid fault system, Saudia Arabia and Egypt: a late Precambrian rift related transform system? Tectonics 4:497–511

Subrahmanyam M, Prakasa Rao TKS (2009) Interpretation of magnetic anomalies using some simple characteristic positions over tabular bodies. Explor Geophys 40:265–276

Tlas M, Asfahani J (2011) Fair function minimization for interpretation of magnetic anomalies due to thin dikes, spheres and faults. J Appl Geophys 75:237–243

Tsokas GN, Papazachos CB (1992) Two-dimensional inversion filters in magnetic prospecting: application to the exploration for buried antiquities. Geophysics 57:1004–1013

Ugbor CC, Emedo CO, Arinze IJ (2021) Interpretation of airborne magnetic and geo-electric data: resource potential and basement morphology of the Ikom-Mamfe embayment and environs, Southeastern Nigeria. Nat Resour Res 30:153–174

Usman N, Lawal KM, Aku MO (2014) Application of werner deconvolution method in the direct interpretation of residual aeromagnetic anomalies. IOSR J Appl Phys 6:18–21

Venter G, Sobieszczanski-Sobieski J (2002) Particle swarm optimization. AIAA J 41:1583–1589

Xiong J, Zhang T (2015) Multiobjective particle swarm inversion algorithm for two-dimensional magnetic data. Appl Geophys 12:127–136